Chapter 2
Introduction to Isotope Effect

2.1 The Nucleons and its Constituents

An atom consists of an extremely small, positively charged nucleus (see Fig. 2.1) surrounded by a cloud of negatively charged electrons. Although typically the nucleus is less than one ten-thousandth the size of the atom, the nucleus contains more than 99.9% of the mass of the atom. Atomic nucleus is the small, central part of an atom consisting of A-nucleons, Z-protons, and N-neutrons (Fig. 2.2). The atomic mass of the nucleus, A, is equal to Z+N. A given element can have many different isotopes, which differ from one another by the number of neutrons contained in the nuclei [1, 2]. In a neutral atom, the number of electrons orbiting the nucleus equals the number of protons in the nucleus. As usually nuclear size is measured in fermis ($1\,\text{fm} = 10^{-15}\,\text{m}$, also called femtometers). The basic properties of the atomic constituents can be read in Table 2.1.

As we can see from Table 2.1, protons have a positive charge of magnitude $e = 1.6022 \times 10^{-19}\,\text{C}$ (Coulombs) equal and opposite to that of the *electron*. *Neutrons* are uncharged. Thus a neutral atom (A, Z) contains Z electrons and can be written symbolically as ${}^{A}_{Z}\text{X}_{N}$ (see also Fig. 2.2). Here X is chemical symbol and N is neutron number and is equal $\text{N} = \text{A} - \text{Z}$. The masses of *proton* and neutron are almost the same, approximately 1836 and 1839 electron masses (m_e), respectively. Apart from electric charge, the proton and neutron have almost the same properties. This is why there is a common name of them: *nucleon*. Both the proton and neutron are nucleons. As we well know the proton is denoted by letter p and the neutron by n. Chemical properties of an element are determined by the charge of its atomic *nucleus*, i.e., by the number protons (electrons). It should be added, that although it is true that the neutron has zero net charge, it is nonetheless composed of electrically charged quarks (see below), in the same way that a neutral atom is nonetheless composed of protons and electrons. As such, the neutron experiences the *electromagnetic interaction*. The net charge is zero, so if we are far enough away from the neutron that it appears to occupy no volume, then the total effect of the electric force will add up to zero. The

V. G. Plekhanov, *Isotope-Based Quantum Information*, SpringerBriefs in Physics,
DOI: 10.1007/978-3-642-28750-3_2, © The Author(s) 2012

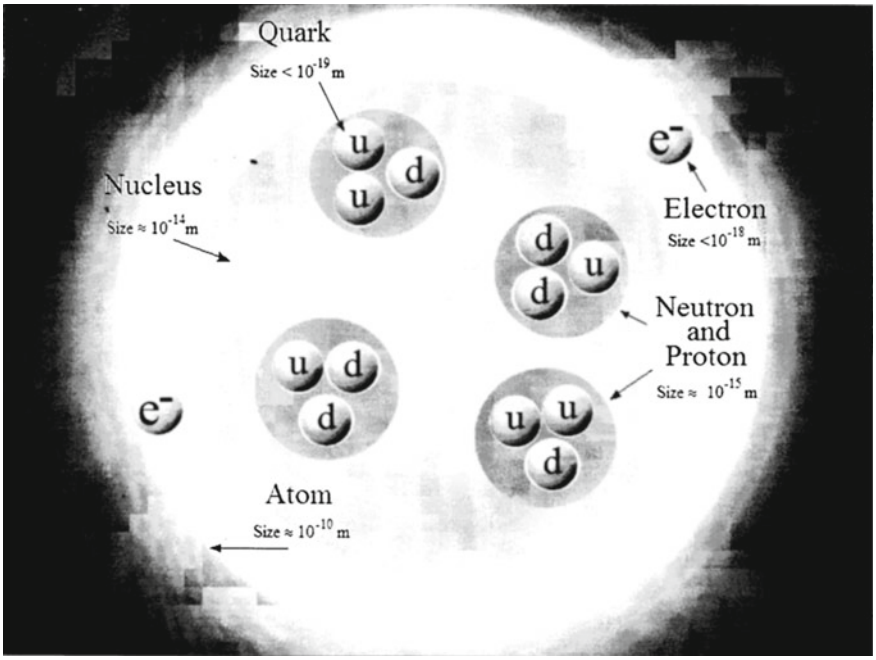

Fig. 2.1 Structure within the atom. If the *protons* and *neutrons* in this picture were 10 cm across, then the quarks and electrons would be less than 0.1 mm in size and the entire atom would be about 10 km across (after http://www.lbl.gov/abc/wallchart/)

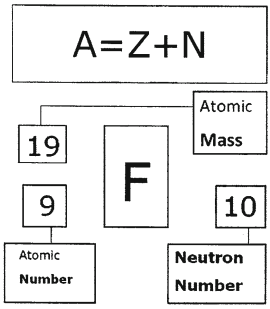

Fig. 2.2 Atomic nomenclature

movement of the charges inside the neutrons does not cancel, however, and this is what gives the neutron its nonzero *magnetic moment*.

Each of the atomic constituents a spin 1/2 in units of $\hbar\,(=\mathrm{h}/2\pi)$ and is an example of the class of particles of half-integer spin known as *fermions*. Fermions obey the exclusion principle of Pauli, which determines the way electrons can occupy atomic energy states. The same rule applies, as will be shown below, to nucleons in nuclei. Associated with the spin is a magnetic dipole moment. Compared with the magnetic moment of *electron*, nuclear moment is very small. However, they play an important

Table 2.1 The basic properties of the atomic constituents

Particle	Charge	Mass (u)	Spin ($\hbar$)	Magnetic moment (JT^{-1})
Proton	e	1.007276	1/2	1.411×10^{-26}
Neutron	0	1.008665	1/2	-9.66×10^{-27}
Electron	−e	0.000549	1/2	9.28×10^{-24}

role in the theory of *nuclear* structure. It may be surprising that the uncharged neutron has a magnetic moment. This reflects the fact that it has an underlying quark substructure (see, e.g. [3]), consisting of charged components. Electron scattering off these basic nuclear constituents (proton and neutron) makes up for the ideal probe to obtain a detailed view of the internal structure. A very detailed analysis using the best available data has been carried out recently by Kelly [4]; these data originate from recoil or target polarizations experiments. In Fig. 2.3 the proton charge and magnetization distribution are given. What should be noted is the softer charge distribution compared to the magnetic one for proton. These resulting densities are quite similar to Gaussian density distributions that can be expected starting from *quark picture* (for details, see below) and, at the same time more realistic than the exponential density distributions [5–10]. The neutron charge and magnetization are also given in Fig. 2.3. What is striking is that magnetization distribution resembles very closely the corresponding *proton* distribution. Since scattering on neutrons normally carries the larger error, the neutron charge distribution is not precisely fixed. Nonetheless, one notices that the interior charge density is balanced by a negative charge density, situated at the neutron surface region, thereby making up for the integral vanishing of the total charge of the *neutron*.

We should recall from atomic physics that the quantity e$\hbar$/2m is called *magneton*. For atomic motion we use the *electron mass* and obtain the Bohr's magneton $\mu_B = 5.7884\times10^{-5}$ eV/T. Putting in the proton mass we have the nuclear magneton $\mu_N = 3.1525\times10^{-8}$ eV/T. Note that $\mu_N \ll \mu_B$ owing to the difference in the masses, thus under most circumstances atomic magnetism has much larger effects than nuclear magnetism. Ordinary magnetic interactions of matter (ferromagnetism, for example) are determined by *atomic magnetism*.
We can write

$$\mu = g_l l \mu_N \tag{2.1}$$

where g_l is the g-factor associated with the orbital angular momentum l. For protons $g_l = 1$, because neutrons have no electric charge; we can use Eq. (2.1) to describe the orbital motion of neutrons if we put $g_l = 0$. We have thus been considering only the orbital motion of *nucleons*. Protons and neutrons, like electrons, as mentioned above also have intrinsic or spin magnetic moments, which have no classical analog but which we write in the same form as Eq. (2.1):

$$\mu = g_s s \mu_N \tag{2.2}$$

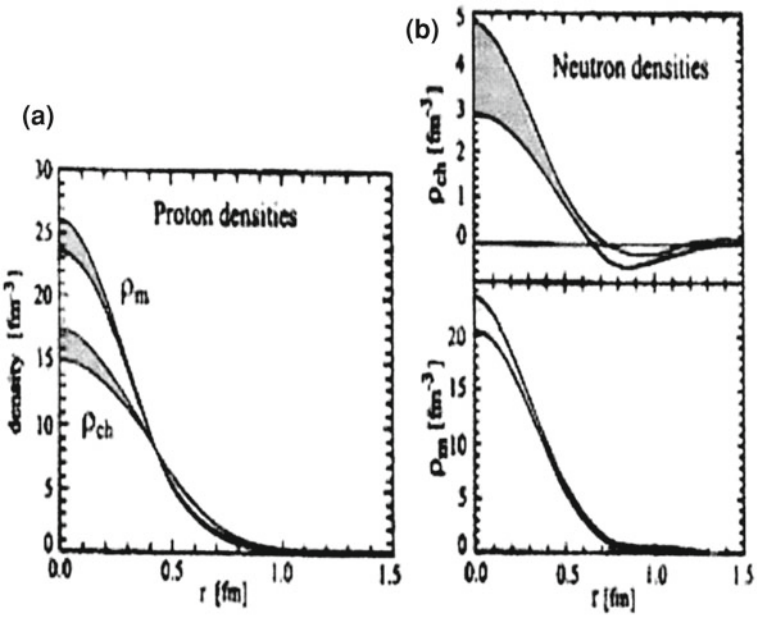

Fig. 2.3 Comparison between charge (ρ_{ch}) and magnetization (ρ_m) for the proton (**a**) and neutron (**b**). Both densities are normalized to $\int \mathrm{d}r r^2 \rho(r) = 1$ (after [5–7])

where $s = 1/2$ for protons, neutrons, and electrons (see Table 2.1). The quantity g_s is known as the spin g-factor and is calculated by solving a relativistic quantum mechanics equation (see, also [8–10]). For free nucleons, the experimental values are far from the expected value for point particles: proton–$g_s = 5.5856912 \pm 0.0000022$ and neutron $-g_s = 3.8260837 \pm 0.0000018$.

2.1.1 Mass and Nuclear Binding Energy

Inside a *nucleus*, neutrons and protons interact with each other and are bound within the nuclear volume under the competing influences of attractive nuclear and repulsive electromagnetic forces. This binding energy has a direct effect on the mass of an atom. It is therefore not possible to separate a discussion of *nuclear binding energy*; if it were, then nucleon would have masses given by $Z_{m_p} + Z_{m_n}$ and the subject would hardly be of interest.

As is well known, in 1905, Einstein presented the equivalence relationship between mass and energy: $E = mc^2$. From this formula, we see that the speed of light c is very large and so even a small mass is equivalent to a large amount of energy. This is why in nuclear physics it is more convenient to use a much smaller unit called megaelectronvolt ($1\,\mathrm{MeV} = 1.602 \times 10^{-13}\,\mathrm{J}$). On the atomic

scale, 1 au is equivalent to 931.5 MeV/c^2, which is why energy changes in atoms of a few electron volt cause insignificant changes in the mass of atom. *Nuclear* energies, on the other hand, are millions of electron volts and their effects on atomic mass are easily detectable. For example, the theoretical mass of $^{35}_{17}$Cl is $17 \times 1.00782503 + 18 \times 1.00866491 = 35.28899389$ amu. Its measured (see below) mass is only 34.96995 amu. Therefore, the mass defect and binding energy of $^{35}_{17}$Cl are

$$\Delta = 0.32014389 \text{ amu.}$$
$$\mathrm{E}_B = \frac{0.32014389 \times 931.5}{35} = 8.520 \text{ MeV/nucleon} \tag{2.3}$$

and in common sense the binding energy is determined by next relation

$$\mathrm{E}_B = \mathrm{Z}m_p + \mathrm{N}m_n - \mathrm{B/c}^2 \tag{2.4}$$

where B/c^2 is the actual nuclear mass.

As we can see, the *binding energy* of the atoms of most elements have values ranging from about 7.5 to 8.8 MeV [11]. The binding energy per nucleon rises slightly with increasing mass number and reaches a maximum value for ^{62}Ni. Thereafter the binding energies decline slowly with increasing mass number. The binding energies of the atoms of H, He, Li, and Be are lower than the binding energies of the other elements (see, also Fig. 2.5 below).

The measurement of *nuclear masses* occupies an extremely important place in the development of nuclear physics. *Mass spectrometry* (see, e.g. [12–15]) was the first technique of high precision available to the experimenter, since the mass of a nucleus increases in a regular way with the addition of one proton or neutron. In mass spectrometers, a flux of identical nuclei (ions), accelerated to a certain energy, is directed to a screen (photoplate) where it makes a visible mark. Before striking the screen, this flux passes through magnetic field, which is perpendicular to velocity of the nuclei. As a result, the flux is deflected to certain angle. The greater the mass, the smaller the angle. Thus, measuring the displacement of the mark from the center of the screen, we can find the deflection angle and then calculate the mass. The example of a mass spectrum of different isotopes of krypton is shown in Fig. 2.4. From the relative areas of the peaks it can determine the abundance of the stable isotopes of krypton (for details see [12–15]).

Relative masses of *nuclei* can also be determined from the results of nuclear reactions or nuclear decay. For example, if a nucleus is radioactive and emits an α-particle, we know from energy conservation that its mass must be greater than that of decay products by the amount of energy released in the decay. Therefore, if we measure the letter, we can determine either of the initial or the final nuclear masses if one of them is unknown. An example of this is presented briefly below. At present we shall illustrate some typical reactions, bridging the gap between "classical" methods and the more advanced "high-energy" types of experiments [4–7].

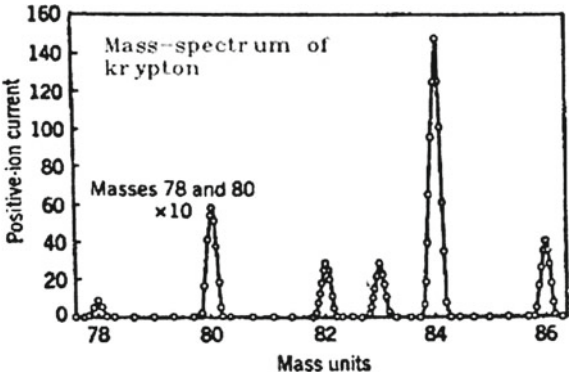

Fig. 2.4 A *mass-spectrum* analysis of krypton. The ordinates for the peaks at mass positions 78 and 80 should be divided by 10 to show these peaks in their true relation to the others (after [11])

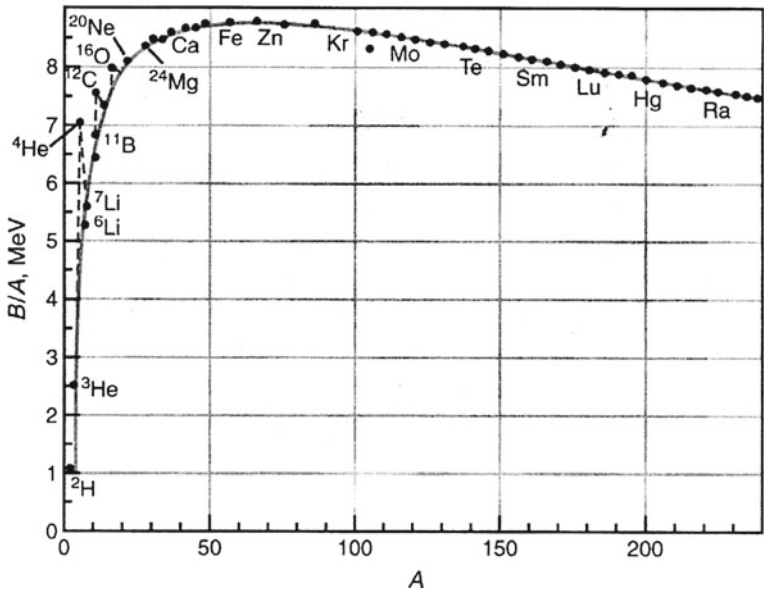

Fig. 2.5 The *binding energy* per *nucleon* B/A as a function of the nuclear mass number A (after [16])

The possible, natural decay processes can also be brought into the class of reaction processes with the conditions: no incoming light particle α and $Q > 0$. We list them in the following sequence:

α-decay:

$$ {}^{A}_{Z}\mathrm{X}_{N} \rightarrow {}^{A-4}_{Z-2}\mathrm{Y}_{N-2} + {}^{4}_{2}\mathrm{He}_{2} \tag{2.5} $$

Table 2.2 Masses of electron, nucleons and some nuclei (after [11])

Particle	Number of protons	Number of neutrons	Mass (MeV)
e	0	0	0.511
p	1	0	938.2796
n	0	1	939.5731
$^{2}_{1}$H	1	1	1876.14
$^{3}_{1}$H	1	2	2808.920
$^{3}_{2}$He	2	1	2808.391
$^{4}_{2}$He	2	2	3728.44
$^{7}_{3}$Li	3	4	6533.832
$^{9}_{4}$Be	4	5	8392.748
$^{12}_{6}$C	6	6	11174.860
$^{16}_{8}$O	8	8	14895.077
$^{238}_{92}$U	92	146	221695.831

β-decay:

$$^{A}_{Z}\mathrm{X}_{N} \rightarrow {}^{A}_{Z-1}\mathrm{Y}_{N+1} + \mathrm{e}^{+} + \nu_e \quad (\mathrm{p} \rightarrow \mathrm{n\text{-}type}) \tag{2.6}$$

$$^{A}_{Z}\mathrm{X}_{N} \rightarrow {}^{A}_{Z+1}\mathrm{Y}_{N-1} + \mathrm{e}^{-} + \overline{\nu}_e \quad (\mathrm{n} \rightarrow \mathrm{p\text{-}type}) \tag{2.6'}$$

$$^{A}_{Z}\mathrm{X}_{N+\mathrm{e}^{-}} + \mathrm{e}^{-} \rightarrow {}^{A}_{Z-1}\mathrm{Y}_{N+1} + \nu_e \quad (\mathrm{e}^{-}\text{-capture}) \tag{2.6''}$$

Here e^{-}, e^{+}, ν_e and $\overline{\nu}_e$ are *electron, positron, neutrino and antineutrino*.
γ-decay:

$$^{A}_{Z}X^{*}_{N} \rightarrow {}^{A}_{Z}\mathrm{X}_{N} + \mathrm{h}\nu \tag{2.7}$$

Here X^{*} is excited nuclei. Nuclear fission:

$$^{A}_{Z}\mathrm{X}_{N} \rightarrow {}^{A_1}_{Z_1}\mathrm{Y}_{N_1} + {}^{A_2}_{Z_2}\mathrm{U}_{N_2} + \mathrm{x{\cdot}n}. \tag{2.8}$$

Since mass and energy are equivalent (see Einstein formula above), in nuclear physics it is customary to measure masses of all particles in the units of energy (MeV). Examples of masses of subatomic particles are given in Table 2.2.

As was noted above, nuclear binding energy increases with the total number of nucleons A and, therefore, it is common to quote the average binding energy per nucleon (B/A). The variation of B/A with A is shown in Fig. 2.5. Several remarkable features are immediately apparent. First of all, the curve is relatively constant except for the very *light nuclei*. The average binding energy of most nuclei is, to within 10%, about 8 MeV per nucleon. Second, we note that the curve reaches peak near $\mathrm{A} = 60$, where the nuclei are most tightly bound, light and very *heavy nuclei* are containing less bound nucleons. Thus, the source of energy production in fusion of light nuclei or fusion of very heavy nuclei can be source of energy [16, 17].

The interactions between two nucleons (NN) is one of the central questions in physics and its importance goes beyond the properties of nuclei. Nucleons can combine to make four different few-nucleon systems, the deuteron ($p + n$), the triton

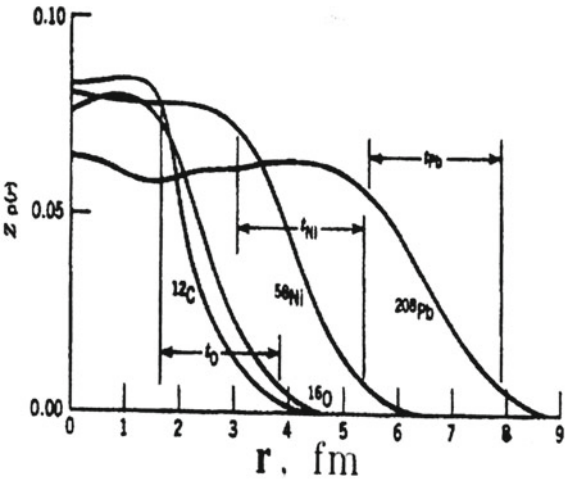

Fig. 2.6 Coulomb potential used for defining the nuclear radius R

$(p + 2n)$, the helion $(2p + n)$ and the α-particle $(2p + 2n)$ (see, e.g. [18–21]). These particles are grouped together because they are stable (excluding from the radioactive triton which has a half-life of about 12 years and so may be treated as a stable entity for most practical purpose), have no bound excited states (except the α-particles which have two excited states at about 20 and 22 MeV), and are frequently used as projectiles in nuclear investigations. The absence of stable particles of mass of five provides a natural boundary between few nucleon systems and heavier nuclei [20]. Few nucleon systems provide the simplest systems to study nuclear structure. The deuteron provides important information about the nucleon–nucleon interaction. Below we have indicated a few of the properties of the N–N force:

1. At short distances it is stronger than the Coulomb's force; the nuclear force can overcome the Coulomb's repulsion (see also Fig. 2.6) of protons in the nucleus.
2. At long distances, of the order of atomic sizes, the nuclear force is negligibly feeble. The interaction among nuclei in a molecule can be understood based only on the Coulomb's force.
3. Some fundamental particles are immune from the nuclear force. At present time we have no evidence from atomic structure, for example, that electrons feel the nuclear force at all.
4. The N–N force seems to be nearly independent of whether the nucleons are neutrons or protons. As is well known this property is called charge independence.
5. The N–N force depends on whether the spins of the nucleons are parallel or antiparallel.
6. The N–N force includes a repulsive term, which keeps the nucleons at a certain average separation.
7. The N–N force has a noncentral or tensor component. This part of the force does not conserve orbital angular momentum, which is a constant of the motion under central forces.

2.2 Manifestation Isotope Effect in Condensed Matter

Studies of vibrational properties of crystals containing impurities (defects of various type [22]) were described in detail in a number of excellent review [23, 24]. The main characteristics of a *phonon* spectrum are the *dispersion* relation $\omega(\vec{q})$ and the frequency distribution function $g(\omega)$ [25]. Both are mainly determined in experiments on the scattering of thermal neutrons, provided it turns out to be possible to separate coherent and incoherent scattering [26]. An important role of neutrons in studying lattice dynamics is related to the fact that the energy of thermal neutrons ($k_B T \sim 10^{-1} - 10^{-2}$ eV) is of the same order as the energy of phonons. At the same time their de Broglie wavelength is comparable with the interatomic distance in crystals [27, 28].

The simplest defects in a crystalline lattice that distort its translational symmetry are *isotopes* of the elements forming a crystal. If the impurity concentration (isotopes) in a crystal is high enough that the interaction between impurity atoms (ions) plays an important role, such a system is called a mixed crystal with a various degree of *disorder*. There are two types of disordered systems: disordered alloys (isotopic mixtures) or mixed crystals and glassy substances, which possess a more pronounced spatial disorder than configurational disorder. The first theoretical dynamic model of mixed crystals was a linear chain, which represented the development of the virtual model (Nordheim, 1931; Pant and Joshi, 1969 (see, e.g. [47])). Despite its simplicity, this model adequately described general features of lattice dynamics of mixed alkali-halide crystals. This model uses two independent force constants f_0 and f_0', which are obtained, as a rule, from the observed frequencies of LO phonons in pure substances, according to the expression $f = \omega^2 mM/2(m+M)$, *where* m and M (M′) are masses of crystal-forming particles. The dependence of the force constant on concentration was described by equation $F = f_0 x - (f_0' - f_0)x$ by assuming a linear dependence of f_0 (f_0') on concentration x (see, also [22] and references therein). A more complex concentration dependence of the force constant was considered in detail in comprehensive reviews [29–33], where the cluster model and isodisplacement model in lattice dynamics, based on the *Coherent Potential Approximation* (CPA) or averaging of the T-matrix, were also described.

2.2.1 Isotope Effect in Phonon Spectra

a. First-order Raman Spectra

In view of the obvious mass dependence of *phonon frequencies*, dynamic lattice properties have been studied intensively, mainly by *Raman scattering*. In addition to changes in the average atomic mass, mass fluctuation due to isotopic disorder as will be shown below also affects phonon frequencies and line-widths. Elemental *semiconductors* (C, Si, Ge, α-Sn) with *diamon-like structure* are an ideal object to

study the isotopic effects by the method of the Raman scattering. At the present time the high-quality isotopically enriched indicated crystals are also available. In this part we describe our understanding of the first-order Raman spectra of the *isotope-mixed elemental and compound semiconductors* (CuCl, GaN, GaAs) with zinc-blend structure.

The materials with *diamond* structure discussed here have a set of threefold-degenerate phonons (frequency ω_0) at the centre ($\overrightarrow{k} = 0$, Γ-point) of the Brillouin zone (BZ) (see, also [26]). These phonons are Raman active but infrared inactive [34]. Let us consider the case of Ge, with the five isotopes [35–37]. The uninitiated will ask himself whether one should see five phonons (or more if he knows that there are two atoms per *primitive cell* (PC)) corresponding to the five different masses, or only one corresponding to the average mass. The reason why the Raman spectrum (see, Fig. 2.7) of natural Ge does not show the local modes of the individual isotopes is that the scattering potentials for the phonons due to the mass-defects (mass fluctuations) are too small to induce bound states (i.e., *Anderson localization* of the phonons [38, 39]). Really a three-dimensional crystal fluctuations in the parameters of the secular equation lead to localization if these fluctuation (measured in units of frequency, i.e., $(\Delta M/M)\omega_0$) are larger than the bandwidth of the corresponding excitations. For optical phonons in Ge this bandwidth is $\sim 100\,\mathrm{cm}^{-1}$ (see, e.g. [40]) while $(\Delta M/M)\omega_0 \leq 0.4 \times 300 = 12\,\mathrm{cm}^{-1}$). Hence no phonon localization (with lines corresponding to all pairs of masses) is expected, in agreement with the observation of only line at $304\,\mathrm{cm}^{-1}$ ($\sim 80\,\mathrm{K}$) for natural Ge.

Figure 2.7a demonstrates the dependence of the shape and position of the first-order line of *optical phonons* in germanium crystals on the isotope composition at liquid nitrogen temperatures [36, 37]. The lines in these spectra are fully resolved instrumentally (the experimental resolution was better than $0.1\,\mathrm{cm}^{-1}$) and their width is caused by homogeneous broadening. The centroid of the *Raman line shifts* following relation $\omega_0 \sim M^{-1/2}$. This behavior is expected within *harmonic approximation*. Additional frequency shifts are observed [41] for the natural and alloy samples which arise from their *isotope* mass disorder. This additional shift is $0.34 \pm 0.04\,\mathrm{cm}^{-1}$ in natural Ge and $1.06 \pm 0.04\,\mathrm{cm}^{-1}$ (Fig. 2.8) in the $^{70/76}$Ge alloy sample, which has nearly the maximum *isotopic disorder* possible with natural isotopes.

As it is well known, the natural diamond exhibits a single first-order Raman's peak at $\omega_{\mathrm{LTO}}(\Gamma) = 1332.5\,\mathrm{cm}^{-1}$. Figure 2.7b shows the first-order *Stokes Raman spectra* for several samples with different isotope ratios [43]. The Raman energy is found to increase continuously, but nonlinear, with decreasing x. The energy difference between the extreme compositions is $52.3\,\mathrm{cm}^{-1}$, which is consistent with the isotope mass ratio. Analogous structures of first-order light scattering spectra and their dependence on isotope composition has now been observed many times, not only in elementary Si [44] and α-Sn [45], but also in compound CuCl and GaN semiconductors (for more details see reviews [45–47]). Already this short list of data shows a large dependence (see, also Fig. 2.8) of the structure of first-order light scattering spectra in *diamond* as compared to other crystals (Si, Ge).

Figure 2.9 compares the composition of the Raman frequency in the *VCA* and *CPA* according to Hass et al. [48] and Spitzer et al. [49]. The present Raman data

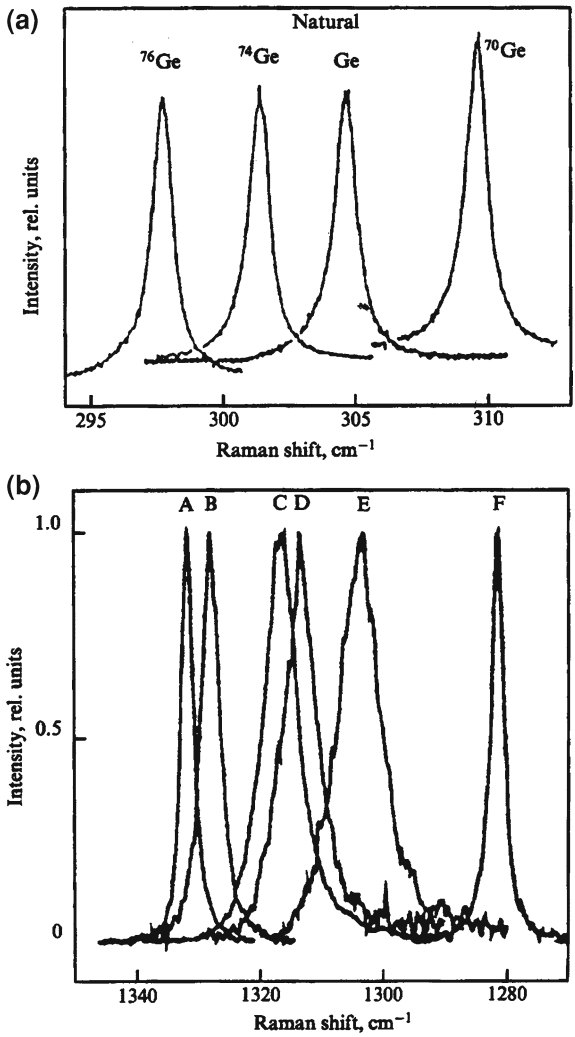

Fig. 2.7 **a** First-order Raman scattering spectra in Ge with different *isotope* contents [36, 37]; **b** First-order Raman scattering spectra in isotopically mixed *diamond* crystals $^{12}C_x^{13}C_{1-x}$. The peaks *A*, *B*, *C*, *D*, *E*, and *F* correspond to x = 0.989; 0.90; 0.60; 0.50; 0.30; and 0.001 [43]

in Fig. 2.9 are in excellent agreement with those of Chrenko [50] and Hanzawa et al. [43]. Both sets of data exhibit a pronounced bowing (nonlinearity) relative to the VCA that is described very well by CPA. Hass et al. concluded that the bowing is a direct consequence of the scattering due to isotopic disorder. Similar nonlinearity are observed in many other properties of alloy systems (e.g., the band gaps of semiconductor alloys and isotope-mixed crystals [51]. The deviation from linearity is approximately 5 cm^{-1}near the middle of the composition range. This is much larger than the experimental uncertainties (about the size of the data points) and should certainly be considered if the Raman frequency is to be used as a measure of *isotopic composition* (for details see [26]).

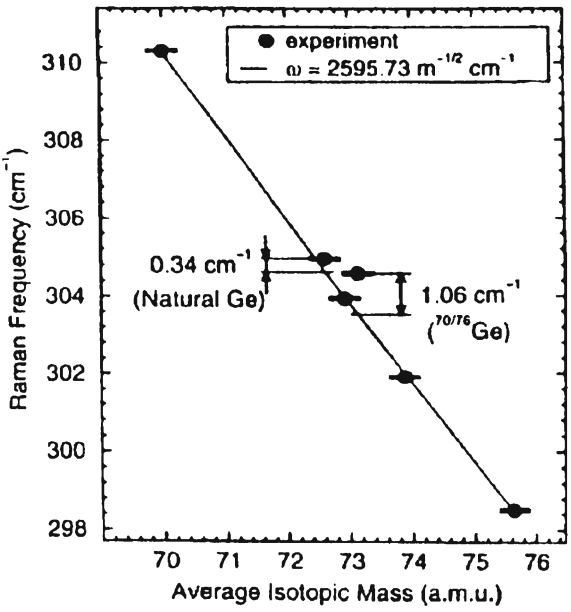

Fig. 2.8 Raman frequency as a function of the average mass, measured at 10 K, for *isotopically enriched* and disordered Ge samples. The *solid line* is a calculation with $\omega = 2595{,}73/\sqrt{\mathrm{M}}\ \mathrm{cm}^{-1}$ (after [41])

The measured Raman linewidth (Fig. 2.9b) is larger near the center of the composition range than near the end points. The variation is not symmetric in x and $(1-\mathrm{x})$ and the maximum width occurs at approximately 70% at ^{13}C. The CPA curves represent intrinsic contributions to the Raman linewidth due to the disorder-induced broadening of the zone-center optic mode. The observed widths, according to Hass et al. [48], contain additional contributions due to instrumental resolution ($\sim 1.8\,\mathrm{cm}^{-1}$) and *anharmonic* decay [47, 51]. The anharmonic broadening of the Raman line has been calculated for diamond by Wang et al. [45] to be on the order of $1\,\mathrm{cm}^{-1}$ at 300 K. Contributions other than disorder thus account well for the observed widths near $x = 0$ and 1. Assuming that such contributions are reasonably constant across the entire composition range, we see that both CPA calculations account very well for the qualitative trend in the data, including the peak near $x = 0.7$.

Detail calculations of the self-energy and the first-order Raman lineshape were performed by Spitzer et al. [49]. They obtained a qualitative agreement with experimental results. Comparing the Raman lineshape of Ge and C, the presence of a large isotopic broadening for *diamond*, contrary to the small broadening observed for Ge should be noted. The reason lies in the fact that $\vec{k} = 0$ is not the highest point of the phonon dispersion relation in the case of diamond [52]. This maximum lies somewhat off $\vec{k} = 0$, resulting in a nonvanishing density of states at ω_0, considerably larger than that found from relation $\mathrm{N}_d \sim \mathrm{Re}\left(\omega_0 - \omega + \mathrm{i}\frac{\Delta\omega_0}{2}\right)^{1/2}$ [46]. This density of states is strongly asymmetric about ω_0, a fact which yields an asymmetric phonon lineshape [49]. This asymmetry also results in a lopsided dependence of

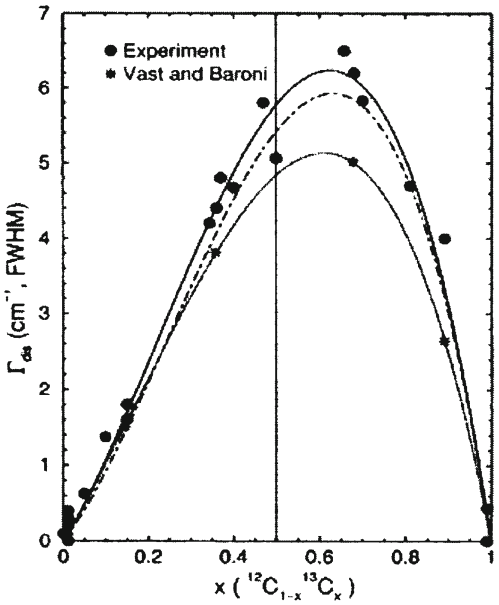

Fig. 2.9 **a** Disorder-induced shift of the Raman phonon of *diamond* as a function of the ^{13}C concentration. The open symbols are Raman experimental data , whereas the asterisks correspond to ab initio calculations. The solid line is a fit with Eq. (2.40) for $n = 2, 3$ to all experimental data [60]. The *dotted* and *dot–dashed lines* represent the fits to theoretical values obtained from ab initio and CPA calculations, respectively (after [69]); *b Disorder-induced broadening* of the Raman phonon of diamond as a function of the ^{13}C concentration. The filled circles have been obtained from the Raman data by taking into account the corresponding instrumental resolutions and substracting the anharmonic broadening $\Gamma_{anh} \approx 2\text{cm}^{-1}$ (FWHM). The solid line is a fit with Eq. (2.40) for $n = 2, 3$ to these points [60]. The *dotted* and *dot–dashed lines* are the corresponding fits to the values obtained from ab initio and CPA calculations, respectively (after [69])

the linewidth versus concentration (Fig. 2.9), which disagrees with the symmetric dependence expected from the proportionality to mass fluctuation parameter g [22].

Thus, depicted in Figs. 2.7–2.9 experimental results are testified the nonlinear dependence Raman frequency shift on the *isotope concentration*.

b. Second-order Raman Spectra

The *second-order* Raman spectra for a natural and isotope-mixed crystals of diamond were investigated by Chrenko [50] and Hass and cowokers [48]. Second-order Raman spectra for the synthetic diamonds are shown in Fig. 2.10 . The second-order spectra were measured by Hass and cowokers with slightly lower resolution ($\sim 4\,\text{cm}^{-1}$) than the first-order spectra because of the much lower count rate. The results of Hass et al. for 1.1 at. % ^{13}C agree well with previous measurements for natural diamond [53]. The spectra for 0.07 and 99 at % ^{13}C also look similar, if one ignores the shifts that

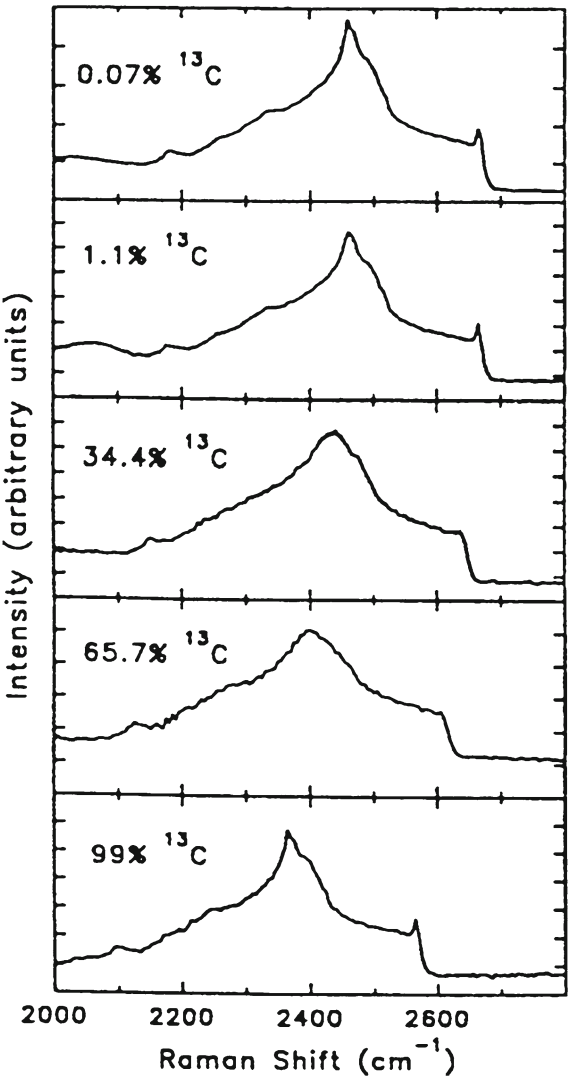

Fig. 2.10 Second-order Raman spectra for *synthetic diamond* with identicated compositions at room temperature (after [48])

occur as a result of differences in M. More significant differences are observed for the more heavily mixed crystals: the 34.4 and 65.7 at % ^{13}C results are noticeably broader and do not appear to exhibit the sharp peak near the high-frequency cutoff. As was shown above, it is this peak at the top of the second-order spectrum (2667 cm $^{-1}$ for 1.1. at % ^{13}C) that has been the subject of intense controversy. Chrenko [50] also examined the second-order spectra of his samples and claims that he was able to see this peak at all composition except 68 % ^{13}C. His measurements may have been of somewhat higher resolution than in paper of Hass et al. but it is clear that even in his

89 at % ^{13}C spectrum (which is the only raw data presented), some broadening of this peak has occurred.

The *IR absorption* in *mixed crystals* can change in two ways, depending on the concentration: *one-mode* and *two-mode* (see, for example, review Elliott et al. [30]). In the case of one-mode behavior, the spectrum always exhibits a single band whose maximum gradually shifts from one extreme position to another. The two-mode behavior corresponds to the presence of two bands in the spectrum, which are characteristic for each of the components of a mixed crystal. As the concentration of components changes, these bands shift, and their intensities undergo a strong redistribution. In principle, the same system can exhibit different types of behavior at the opposite ends [29]. This classification is only a qualitative one, and it is seldom realized in its pure form (for details see review [22]). The appearance of the *localized mode* in the limit of the isolated defect is considered the most important necessary condition for the two-mode behavior of phonons (and also for electrons [32]). In review of Elliott et al. [30], a simple quantitative criterion was suggested for determining the type of behavior of the IR absorption in a crystal of NaCI type [32]. Because the square of the frequency of the TO (Γ) phonon is inversely proportional to the reduced mass of the unit cell M, the shift caused by the defect is equal to

$$\Delta = \omega_{TO}^2 (l - \bar{M}/\bar{M}') \tag{2.9}$$

This shift is compared in paper of Elliott and others with the width of the phonon optical zone. This width in the parabolic dispersion approximation, neglecting the acoustic branches, is equal to

$$\mathrm{W} = \omega_{TO}^2 \frac{\varepsilon_0 - \varepsilon_\infty}{\varepsilon_0 + \varepsilon_\infty}. \tag{2.10}$$

The localized or gap mode appears provided $|\Delta| > \mathrm{W}/2$. However, as was noted by Elliott et al. [30], in order for the two peaks to be retained up to a concentration of about 0.5, the stricter condition of $|\Delta| > \mathrm{W}$ should be satisfied. The substitution of numerical values into (2.9) and (2.10) shows that the relation

$$|\Delta| > \frac{1}{2}\mathrm{W} \tag{2.11}$$

for LiH (LiD) is always valid, because $|\Delta| = 0.44\omega_{TO}^2$ and $\mathrm{W} = 0.58\omega_{TO}^2$. This means that the *localized mode* should be observed at low concentrations. This conclusion agrees with the experimental data described above (Fig. 26 in Ref. [22]). As for the second theoretical relation $|\Delta| > \mathrm{W}$, as noted above, for LiH (LiD) crystals, the reverse relation $\mathrm{W} > |\Delta|$ is always valid [54, 55]. We will consider this question in more detail in review [22]. Figure 2.11 shows the second-order Raman spectra of mixed $\mathrm{LiH}_x\mathrm{D}_{1-x}$ crystals at room temperature [54, 55]. Along with the properties of Raman spectra at high concentrations discussed in the review of Plekhanov [56], note also that as the hydrogen concentration further increases ($x > 0.15$), the

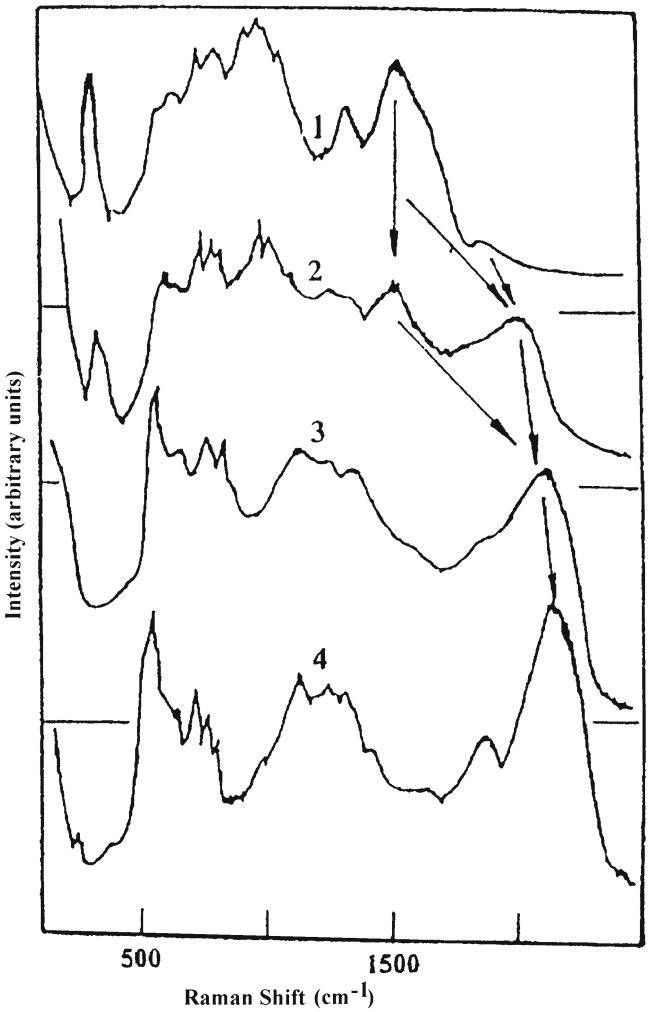

Fig. 2.11 Second-order Raman spectra of mixed LiH_xD_{1-x} crystals excited at λ + 488.0 nm at room temperature, x = 0.0 (*1*); x = 0.42 (*2*); x = 0.76 (*3*); x = 1 (*4*). The *arrows* show the bands corresponding to LO(Γ) phonons (after [54, 55])

intensity of the 2LO (Γ) phonon peak in a LiD crystal decreases, while the intensity of the highest frequency peak in mixed LiH_xD_{1-x} crystals increases. The latter peak is related to the renormalized LO (Γ) modes in a mixed crystal. Thus, comparison of Raman spectra 1 and 2 in Fig. 2.11 shows that in the concentration range of $0.1 < x < 0.45$, the Raman spectrum exhibits LO (Γ) phonon peaks of a pure LiD and mixed LiH_xD_{1-x} crystal. A further increase in $x > 0.45$ is accompanied by two effects observed in the Raman spectra of mixed crystals. The first effect is manifested in a substantial rearrangement of the acousto-optical part of the spectrum

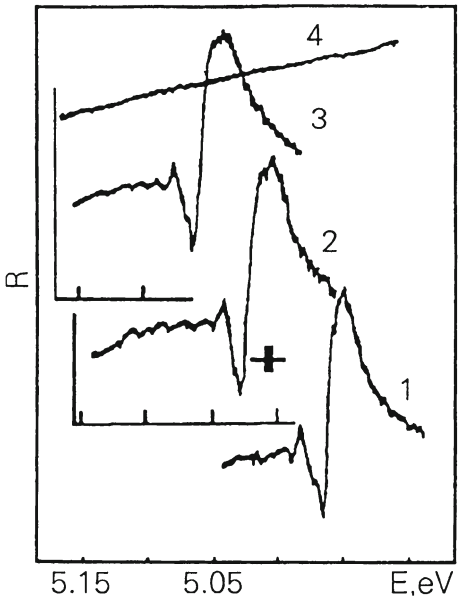

Fig. 2.12 Mirror *reflection* spectra of crystals: 1-LiH; 2-LiH_xD_{1-x}; 3-LiD at 4,2 K. Light source without crystals, curve 4 (after [57])

(spectra 1–3 in Fig. 2.11), and the second one consists in a further blue shift of the highest frequency LO (Γ) phonon peak. This peak shifts up to the position of peak 12 in the spectrum of a pure LiH crystal [56]. This is most clearly seen from comparison of spectra 2 and 4 in Fig. 2.11 (for details see reviews [22, 56]).

2.2.2 Renormalization of Electron (Exciton) States

In this section we will briefly discuss the variation of the *electronic gap* (E_g) and *exciton binding energy* of *insulating* and *semiconducting* crystals with isotope composition. As is well known *isotopic substitution* only affects the wavefunction of phonons; therefore, the energy values of electron levels in the Schrödinger equation ought to have remained the same. This, however, is not so, since isotopic substitution modifies not only the phonon spectrum, but also the constant of electron–phonon interaction. It is for this reason that the energy values of purely electron transition in molecules of hydride and deuteride are found to be different. This effect is even more prominent when we are dealing with a solid [57]. Intercomparison of *absorption* spectra for thin films of LiH and LiD at room temperature [58] revealed that the long-wave maximum (as we know now, the exciton peak) moves 64.5 meV toward the shorter wavelengths when H is replaced with D.

The mirror *reflection* spectra of mixed and pure LiD crystals cleaved in liquid helium are presented in Fig. 2.12. For comparison, on the same diagram we have

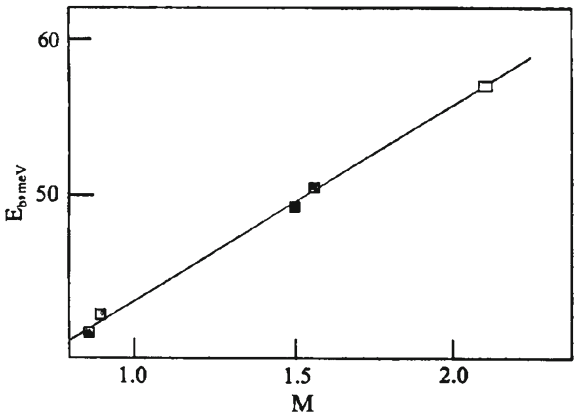

Fig. 2.13 Binding energy of Wannier–Mott excitons as a function of *reduced mass* of ions. Based on values of the reduced mass of ions for ^{6}LiH; ^{6}LiD; ^{7}LiH; ^{7}LiD and ^{7}LiT (after [57])

also plotted the reflection spectrum of LiH crystals with clean surface. All spectra have been measured with the same apparatus under the same conditions. As the *deuterium* concentration increases, the long-wave maximum broadens and shifts toward the shorter wavelengths. As can clearly be seen in Fig. 2.12, all spectra exhibit a similar long-wave structure. This circumstance allows us to attribute this structure to the excitation of the ground (1*s*) and the first excited (2*s*) *exciton* states. The energy values of exciton maxima for pure and mixed crystals at 2 K are presented in Table 21 of Ref. [51]. The binding energies of excitons E_b, calculated by the hydrogen-like formula, and the energies of interband transitions E_g are also given in Table 21 of Ref. [51].

Going back to Fig. 2.12, it is hard to miss the growth of Δ_{12} , [57], which in the *hydrogen-like model* causes an increase of the exciton Rydberg with the replacement of isotopes (see Fig. 2.13). When hydrogen is completely replaced with deuterium, the exciton Rydberg (in the Wannier–Mott model) increases by 20% from 40 to 50 meV, whereas E_g exhibits a 2% increase, and at $2 \div 4.2$ K is $\Delta E_g = 103$ meV. This quantity depends on the temperature, and at room temperature is 73 meV, which agrees well enough with $\Delta E_g = 64.5$ meV as found in the paper of Kapustinsky et al. [58].

The dependence of the *exciton binding energy* on the *isotope* mass presents in Fig. 2.13. From Fig. 2.13 we see that when hydrogen is completely replaced with deuterium, the binding energy of the exciton exhibits a 20% increase from 42 to 52 meV [51]. It is easy to see that in the model of virtual crystal the binding energy of the exciton in LiT crystals must be equal to 57 meV (see Fig. 2.13). Hence it follows that in the linear approximation the isotopic dependence of binding energy of Wannier–Mott excitons may be expressed as

$$E_b = E_b(0)\,(1 + \gamma)\,, \tag{2.12}$$

where $E_b(0)$ is purely the coulombic binding energy of the exciton (in the *frozen lattice*), which in our case is equal to 31.5 meV, and the angular coefficient is $\beta = 12.18\,\text{meV/M}$, where M is the *reduced mass* of ions of lithium and hydrogen (deuterium, tritium) ions; $\gamma = \beta M/E_b\,(0)$ (see also Plekhanov [51]). From the standard equation for the *Coulomb's binding energy* of the exciton

$$E_b = \frac{e^4 \mu}{\hbar^2 \varepsilon_\infty^2}, \tag{2.13}$$

we get the dimensionless constant of the Coulomb's interaction:

$$\eta^2 = \frac{E_b\,(0)}{\hbar\omega_{LO}} = 0.47. \tag{2.14}$$

Comparing the value of $\eta^2 = 0.47$ and the constant of *Fröhlich exciton–phonon interaction* $g^2 = 0.33$ [51] we see that they are close enough. This implies that both the Fröhlich and the Coulomb interactions between electrons (holes) and LO phonons in exciton must be treated with equal attention, as has already been emphasized in Klochikhin's paper [59]. This paper deals from the start with 'bare' *electrons* and *holes*, and all renormalizations are calculated in the two-particle configuration. Such an approach enables us to avoid the considerable difficulty which arises when polarons [60] are used as start-up particles. This difficulty is primarily associated with the fact that the momentum of each particle is conserved when the particles are treated separately, whereas it is the center-of-mass momentum that is conserved when a pair moves as a whole. As demonstrated in Klochikhin [59], this approach also makes it possible to calculate the higher order corrections to the exciton–phonon interaction. It was also shown that the use of the pole parts of polaron *Green functions* in place of complete expressions leads to a situation when the corrections of the order of $\eta^2 g^2$ and g^4 to the potential energy are lost because the corrections to the vertex parts and Green functions cancel out. The quantity lost is of the same order (g^2) as the correction to the residue but has the opposite sign [60]. The approach developed in Klochikhin [59] allowed the calculation of corrections of the order $\eta^2 g^2$ and g^4, the latter is comprised of the correction to the Fröhlich vertex and the correction to the Green functions in the exciton–phonon loop. It is important that the latter have opposite sign and cancel out exactly in the limit $E_b \ll \hbar\omega_{LO}$. As a result, because of the potential nature of the start-up Coulomb interaction, the correction to the Coulomb's vertex of the order $\eta^2 g^2$ does not vanish. As a result, the following expression was obtained in Klochikhin's paper for the binding energy E_b of Wannier–Mott *exciton* when $E_b \ll \hbar\omega_{LO}$ (the spectrum of exciton remains hydrogen like):

$$E_b = \hbar\omega_{LO}\left[\frac{\eta^2 - g^2 + \eta^2 g^2\,(c + v)}{2}\right]^2 \tag{2.15}$$

where c, v = $(m_{c,v}/\mu)^{1/2}$, and m_c, m_v are the electron and hole masses. Now E_b depends explicitly on g^2 (the Fröhlich constant of exciton–phonon interaction), and hence depends on the isotopic composition of the lattice, whereas the standard expression for the binding energy $E_b = \hbar\omega_{LO}\left(\eta^2 - g^2\right) = e^4\mu/\varepsilon_0^2\,\hbar^2$, which describes the exciton spectrum of many semiconductors accurately enough, exhibits no dependence on the isotopic effect. In the case of Eq. (2.15) the exciton spectrum remains hydrogen like. When the higher order corrections are taken into account, Eq. (2.15) becomes

$$E_b = \frac{e^4\mu}{2\varepsilon_0\hbar^2}\left[1 + g^2\varepsilon_0\frac{m_c+m_v}{\varepsilon_\infty} + g^4\frac{\varepsilon_0}{\varepsilon_\infty}\left(\zeta_1+\zeta_2\frac{1-\varepsilon_\infty}{\varepsilon_0}\right)(m_c+m_v)\right]. \qquad (2.16)$$

The order-of-magnitude evaluation of the coefficients ζ_1, ζ_2 gives $\zeta_1 \approx 0.15$ and $\zeta_2 \approx 0.02$; when $g^2(m_c + m_v) \ll 3.3$, the correction of the order $\eta^2 g^4$ is much less than the term of the order $\eta^2 g^2$ (see, e.g. [51] and references therein). Setting $m_v/m_c = 3.5$ and $g^2/\eta^2 = I - \varepsilon_0/\varepsilon_\infty$, and $(\varepsilon_\infty/\varepsilon_0) = (\omega_{TO}/\omega_{LO}) = 1/3.5)$, in paper [59] it was found that E_b $_{(theor)} = 48$ and 42 meV for LiD and LiH, respectively. Comparing these results with the experimental values (see Table 21 of Ref. [51]) we observe good agreement between theory and experiment. Hence follows a natural conclusion that the isotopic dependence of the *exciton binding energy* is primarily due to the *Fröhlich interaction* mechanism between excitons and phonons.

The single-mode nature of exciton reflection spectra of mixed crystals LiH_xD_{1-x} agrees qualitatively with the results obtained with the *virtual crystal model* (see e.g. Elliott et al. [30]; Onodera and Toyozawa [61, 62]), being at the same time its extreme realization, since the difference between ionization potentials ($\Delta\zeta$) for this compound is zero. According to the virtual crystal model, $\Delta\zeta = 0$ implies that $\Delta E_g = 0$, which is in contradiction with the experimental results for LiH_xD_{1-x} crystals. The change in E_g caused by *isotopic substitution* has been observed for many broad-gap and narrow-gap *semiconductor* compounds.

All of these results are documented in Table 21 of Ref. [51], where the variation of E_g, E_b, is shown at the isotope effect. We should highlight here that the most prominent isotope effect is observed in LiH crystals, where the dependence of $E_b = f(C_H)$ is also observed and investigated. To end this section, let us note that E_g decreases by 97 cm^{-1} when ^{7}Li is replaced with ^{6}Li.

Further, we will briefly discuss of the variation of the *electronic gap* (E_g) of *semiconducting* crystals with its isotopic composition. In the last time, the whole row of semiconducting crystals were grown. These crystals are diamond, copper halides, germanium, silicon, CdS, and GaAs. All numerated crystals show the dependence of the electronic gap on the isotope masses (see, reviews [60, 96]).

Before we complete the analysis of these results we should note that before these investigations, studies were carried out on the *isotopic effect* on exciton states for a whole range of crystals by Kreingol'd et al. (see, also [51]). First, the following are the classic crystals Cu_2O [63, 64] with the substitution $^{16}O \rightarrow {}^{18}O$ and $^{63}Cu \rightarrow {}^{65}Cu$. Moreover, there have been some detailed investigations of the isotopic

effect on ZnO crystals , where E_g was seen to increase by $55\,cm^{-1}$ ($^{16}O \rightarrow {}^{18}O$) and $12\,cm^{-1}$ (at $^{64}Zn \rightarrow {}^{68}Zn$) [65, 66]. In [67] it was shown that the substitution of a heavy ^{34}S isotope for a light ^{32}S isotope in CdS crystals resulted in a decrease in the *exciton Rydberg* constant (E_b), which was explained tentatively by the contribution from the nearest electron energy bands, which however are absent in LiH crystals.

More detailed investigations of the exciton *reflectance* spectrum in CdS crystals were done by Zhang et al. [68]. Zhang et al. studied only the effects of Cd substitutions, and were able to explain the observed shifts in the *bandgap* energies, together with the overall temperature dependence of the bandgap energies in terms of a two-oscillator model provided that they interpreted the energy shifts of the *bound excitons* and $n = 1$ polaritons as a function of average S mass reported as was noted above, earlier by Kreingol'd et al. [67] as shifts in the bandgap energies. However, Kreingol'd et al. [67] had interpreted these shifts as resulting from isotopic shifts of the free *exciton binding energies* (see, also [51]), and not the band gap energies, based on their observation of different energy shifts of features which they identified as the $n = 2$ free exciton states (for details see [67]). The observations and interpretations, according Meyer at al. [69], presented by Kreingol'd et al. [67] are difficult to understand, since on the one hand a significant bandgap shift as a function of the S mass is expected [68], whereas it is difficult to understand the origin of the relatively huge change in the free exciton binding energies which they claimed. Meyer et al. [69] reexamine the optical spectra of CdS as function of average S mass, using samples grown with natural Cd and either natural S ($\sim$95% ^{32}S), or highly enriched (99% ^{34}S). These author observed shifts of the bound excitons and the $n = 1$ free exciton edges consistent with those reported by Kreingol'd et al. [67], but, contrary to their results, Meyer et al. observed essentially identical shifts of the free exciton excited states, as seen in both *reflection* and *luminescence* spectroscopy. The reflectivity and photoluminescence spectra in polarized light ($\vec{E} \perp \vec{C}$) over the A and B exciton energy regions for the two samples depicted in Fig. 2.14. For the $\vec{E} \perp \vec{C}$ polarization used in Fig. 2.14 both A and B excitons have allowed transitions, and therefore reflectivity signatures. Figure 2.14 also reveals both reflectivity signatures of the $n = 2$ and 3 states of the A exciton as well as that of the $n = 2$ state of the B exciton.

In Table 2.3 Meyer et al. summarized the energy differences $\Delta E = E(Cd^{34}S) - E(Cd^{nat}S)$, of a large number of bound exciton and free exciton transitions, measured using *photoluminescence*, absorption, and *reflectivity* spectroscopy, in CdS made from natural S ($Cd^{nat}S$, 95% ^{32}S) and from highly isotopically enriched ^{34}S ($Cd^{34}S$, 99% ^{34}S) [51]. As we can see, all of the observed shifts are consistent with a single value, $10.8 \pm 0.2\,cm^{-1}$. Several of the donor bound exciton photoluminescence transitions, in paper [69] can be measured with high accuracy, reveal shifts which differ from each other by more than the relevant uncertainties, although all agree with the $10.8 \pm 0.2\,cm^{-1}$ average shift. These small differences in the shift energies for donor *bound exciton* transitions may reflect a small isotopic dependence of the donor binding energy in CdS. This value of $10.8 \pm 0.2\,cm^{-1}$ shift agrees well with the value of $11.8\,cm^{-1}$ reported early by Kreingol'd et al. [67] for the $B_{n=1}$ transition,

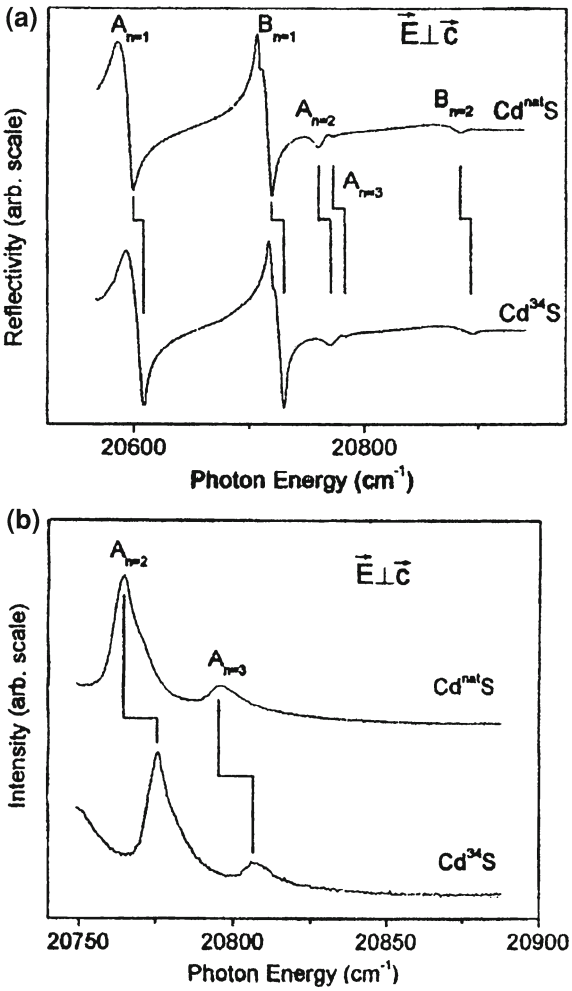

Fig. 2.14 **a** Reflection spectra in the A and B excitonic *polaritons* region of $Cd^{nat}S$ and $Cd^{34}S$ at 1.3 K with incident light in the $\vec{E} \perp \vec{C}$. The *broken vertical lines* connecting peaks indicate measured ene rgy shifts reported in Table 2.3. In this polarization, the n = 2 and 3 excited states of the A exciton, and the n = 2 excited state of the B exciton, can be observed. **b** Polarized photoluminescence spectra in the region of the $A_{n=2}$ and $A_{n=3}$ free exciton recombination lines of $Cd^{nat}S$ and Cd ^{34}S taken at 1.3 K with the $\vec{E} \perp \vec{C}$. The *broken vertical lines* connecting peaks indicate measured energy shifts reported in Table 2.3 (after [69])

particularly when one takes into account the fact that enriched ^{32}S was used in that earlier study, whereas Meyer et al. have used natural S in place of an *isotopically enriched* Cd^{32} S (for details see [51, 69]).

Authors [69] conclude that all of the observed shifts arise predominantly from an *isotopic dependence* of the band gap energies, and that the contribution from any isotopic dependence of the free exciton binding energies is much smaller. On the basis of the observed temperature dependencies of the excitonic transitions energies, together with a simple two-oscillator model, Zhang et al. [68] earlier calculated such a difference, predicting a shift with the S isotopic mass of 950 μeV/amu for the A exciton and 724 μeV/amu for the B exciton. Reflectivity and photoluminescence study of $^{nat}Cd^{32}S$ and $^{nat}Cd^{34}S$ performed by Kreingol'd et al. [67] shows that for

Table 2.3 The energy shifts of all of the transitions studied in [56] are given in terms of the $Cd^{34}S$ minus the $Cd^{nat}S$ energy, ΔE

Transition	Method	ΔE (cm^{-1})
I_2	PL	10.6 ± 0.1
I_2^z	PL	11.1 ± 0.1
I_2^a	PL	10.6 ± 0.1
$A_{n=1}$ (Γ_6)	A$\parallel$	10.8 ± 0.2
$A_{n=1}$ (Γ_5^L)	PL	11.0 ± 0.2
$A_{n=1}$ (Γ_5^L)	R$\perp$	10.9 ± 0.2
$A_{n=2}$	PL$\parallel$	11.3 ± 0.4
$A_{n=2}$	PL$\perp$	11.1 ± 0.4
$A_{n=2}$	R$\perp$	10.2 ± 0.5
$A_{n=3}$	PL$\parallel$	11.8 ± 1.1
$A_{n=3}$	PL$\perp$	10.9 ± 0.6
$A_{n=3}$	R$\perp$	10.7 ± 0.6
$B_{n=1}$ (Γ_1)	R$\parallel$	10.9 ± 0.3
$B_{n=1}$ ($\Gamma_5^L + \Gamma_5^T$)	R$\perp$	10.6 ± 0.4
$B_{n=2}$	R$\parallel$	9.4 ± 1.2
$B_{n=2}$	R$\perp$	9.8 ± 1.2
$C_{n=1}$ (Γ_1)	R$\parallel$	15 ± 6
$C_{n=1}$ (Γ_5)	R$\perp$	14 ± 5

The methods used were photoluminescence spectroscopy (*PL) and reflection spectroscopy (R). For measurements made using polarized light, the $\parallel$ or $\perp$ specifies the orientation of the **E** vector vesus the c axis

anion isotope substitution the ground state ($n = 1$) energies of both A and B excitons have a positive energy shifts with rate of $\partial E/\partial M_S = 740\,\mu$ eV/amu. Results of Meyer et al. [69] are consistent with a shift of $\sim 710\,\mu$eV/amu for both A and B excitons. Finally, it is interesting to note that the shift of the *exciton* energies with Cd mass is $56\,\mu$eV/amu [68], an order of magnitude less than found for the S mass.

In concluding this part we should note that recent high-resolution spectroscopic studies of excitonic and impurity transition in high-quality samples of isotopically enriched Si have discovered the broadening of bound exciton emission (absorption) lines connected with isotope-induced disorder as well as depend on their binding energy on the isotope mass [70–75]. The last effect was early observed on the bound excitons in diamond [56, 51], and earlier on the *free excitons* [76] in $LiH_x\ D_{1-x}$ mixed crystals (see, e.g. [77] and references therein).

2.3 Isotope Low-Dimensional Structure

The advances in epitaxial thin film homo and hetero-structures synthesis, which have been achieved through a variety of *epitaxial* techniques [78–80], have led to a vast array of new solid-state structures with many fascinating properties (see, e.g. [81–83]). *Isotope hetero-structures* has been studied only in last two

decades [81–89]. In combination with the well-established *neutron transmutation* doping (NTD [90]) technique, isotope hetero-structures appear to represent a family of solid-state structures, which offer new possibilities and numerous advantages over the traditional multilayer structures (see above). The formation of a doped *isotope* multilayer structure can be broken down into two independent steps: growth of the structure with isotopically pure or deliberately mixed layers and selective doping with the NTD process [93–95]. The formation of an isotope multilayer structure differs from the traditional methods in only that isotopically pure and deliberately mixed sources must be used, and, the most important, that no dopants are introduced during the growth process. The absence of any dopants during the growth process automatically eliminates all dopant-induced effects including autodoping and dopant interdiffusion between adjacent layers [88]. In principle all the established epitaxial techniques can be applied to the growth of isotope multilayer structures. The only requirement is the availability of *semiconductor* grade pure isotopes. The doping of an isotope heterostructures is achieved with the NTD [90] techniques after growth process has been completed. The NTD technique is isotope selective and therefore it can be used superlatively for the creation of the low-dimensional structure. The *cross-section* for thermal neutron capture and the subsequent nuclear processes of practically every stable isotope of all elements have been measured, studied, and documented (see also [90] and references therein).

As we all know breaking the crystal *translational* symmetry without strongly influencing its *electronic* band structure can be done by means of a modification in the mass of one or more atoms composing the crustal. Without translational symmetry, the wave vector conservation requirements can be circumvented. Ideal models for most studies of elementary excitations are represented by isotopically pure crystals. A new field offering interesting physical studies is opened with the growth of isotopically tailor-made single crystals. The translational symmetry operations can be removed in part by artificial fabricating isotopic superlattice in which layers of two isotopically enriched materials alternate periodically. MBE of *isotopically controlled* germanium has enabled studies of low-dimensional *phonons* in *isotope superlattice* [86–89] and *quantum dots* [91].

In this paragraph we describe the results of Raman measurements on novel kind of heterostructures, a series of isotopic superlattice' of germanium and silicon [86–91]. These samples represent an excellent model system to study the vibrionic properties of superlattice because the electronic structure should be affected only weakly by changes in the isotopic mass (see, e.g. reviews [60, 96]).

Since these changes are the only difference between the superlattice' constituents, *Raman spectroscopy* is the only non-destructive method to investigate their structural properties. Experimental data are compared with the results of planar force-constant model [86]. Let us consider the case of Ge, with the five *isotopes* of it [29]. The readers will ask themselves one should see five phonons (or more if they know that there are two atoms per primitive cell), corresponding to the five different masses, or only one corresponding to the average mass. We all know that the latter is true. The transition from the average mass vibrations to those localized at all possible pairs is an example of the *Anderson localization* phenomenon [38, 39], which is

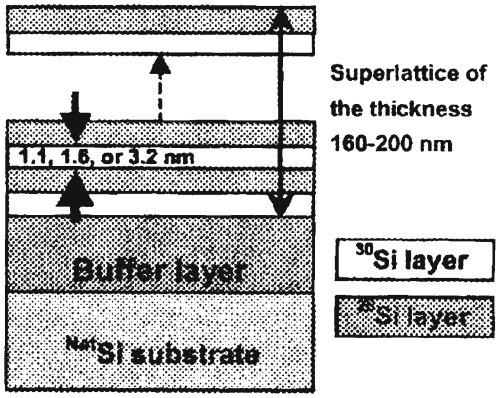

Fig. 2.15 Schematics of Si *isotope superlattices*. Thickness of each isotope layer are 1.1; 1.6; and 3.2 for $^{28}Si_8/^{30}Si_8$; $^{28}Si_{12}/^{30}Si_{12}$ and $^{28}Si_{24}/^{30}Si_{24}$ samples, respectively. Low index denotes the thickness of each isotope layer in atomic monolayers, each 0.136 nm thick (after [92])

observed in Raman experiments on LiH_xD_{1-x} system (for details see [47]). In a three-dimensional crystal, fluctuations in the parameters of the secular equation lead to localization (measured in units of frequency, i.e. $(\Delta M/M)\omega_0$) are larger than the bandwidth of the corresponding excitations. For optical phonons in Ge this bandwidth is $100\,cm^{-1}$ while $(\Delta M/M)\omega_0 \leqslant 0.04 \times 300 = 12 cm^{-1}$ (see also above). Hence no phonon localization (with lines corresponding to all pairs of masses) is expected, in agreement with the observation of only one line at $304\,cm^{-1}$ (at 77 K) for natural Ge (see Fig. 2.7). For comparison we indicate that the bandwidth in the LiH_xD_{1-x} mixed crystal is more than $500\,cm^{-1}$, therefore, the *crystal* and *localized phonons* are coexist (for details see [47]).

In *superlattice* composed, for example, of n layers of ^{70}Ge and m layers of ^{76}Ge repeated periodically, one would expect to find optical modes localized or nearly localized in each of two constituents. Schematics of Si isotope superlattice are depicted in Fig. 2.15 [92]. Koijma et al. have grown three kinds of silicon isotope superlattice ($^{28}Si_n/^{30}Si_n$, with n = 8, 12 and 24) using the solid-source MBE technique [79, 97]. In this paper n denotes the thickness of each isotope layer in atomic monolayers, each 0.136 nm thick. The periodicity, i.e., the number $^{28}Si/^{30}Si$ pair layers stacked vertically, is 80, 50, and 30 for n = 8, 12, and 24 samples, respectively. The resulting total thickness of the superlattice is 160–200 nm (see, Fig. 2.15). The source for the ^{28} Si layer is actually ^{nat}Si which is composed of 92.2% ^{28}Si. The source for the ^{30}Si layer is a single Si crystal isotopically enriched to ^{30}Si(~98.74% [93–95]). In MBE, individual effusion cells equipped with crucibles made of high purity tantalum. The crucible are temperature is maintained at 1400° C for a growth rate of ~0.01 nm/s. The base pressure of the vacuum is 5×10^{-10} torr and the pressure during growth is $\sim 10^{-9}$ Torr Fig. 2.15.

As was shown [98], the E versus k dispersion of *phonons* in the superlattice is *zone folded* due to the new periodicity, na, introduced by the $(^{28}Si)_n$–$(^{30}Si)_n$ unit where a is the periodicity of the bulk Si. Because Raman spectroscopy, to first order, probes phonons situated at k ~ 0 in the dispersion relation, while only one longitudinal optical (LO) phonon peak is observed with bulk Si, multiple LO phonon peaks

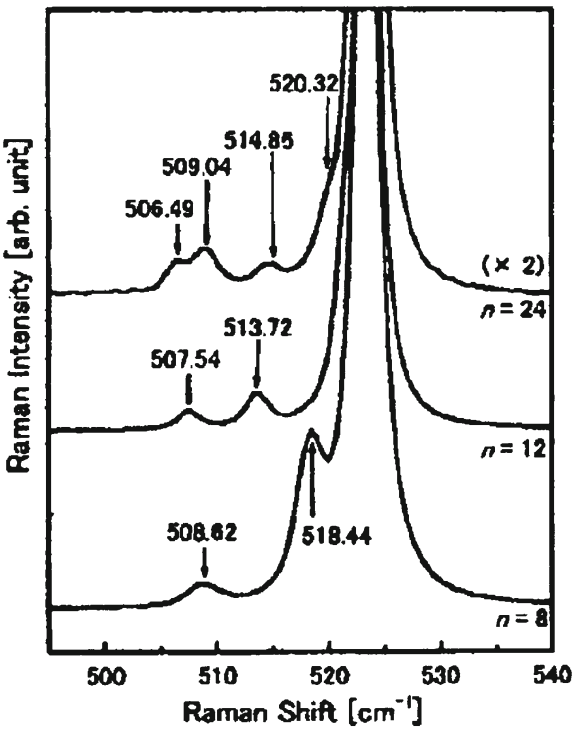

Fig. 2.16 Raman spectra of the $^{28}Si_n/^{30}Si_n$ samples with $n = 8$, 12 and 24 (after [92])

should appear for isotope superlattice due to the zone folding or *phonon localization* (see, e.g. [99]). Figure 2.16 shows the Raman spectra of Si superlattice. As expected, many peaks are observed on the shoulders of the large ^{nat}Si substrate LO peak around 523.5 cm^{-1}. The wave numbers of the identified peaks are indicated in Fig. 2.16 for comparison with theoretical predictions fulfilled in the planar bond-charge model for Si (see [100]). As was shown in paper [93–95] theoretical curves are not smooth due to anticrossings. In general, the agreement between the experimental and theoretical results is excellent, except for the one detail: while LO_1 (^{28}Si) peaks in n = 12 and 24 samples are hidden in the large substrate peak, the LO_1 (^{28}Si) peak is observed experimentally for the n = 8 sample and its position deviates from the calculation (for details see Fig. 4 in [92]).

Raman spectra of a serial of isotopic $^{70}(Ge)_n^{74}(Ge)_n$ *superlattice* with $2 \leq n \leq 32$ ($8 \leq n \leq 24$) was published in papers [87, 88]. Three modes could be observed (see Fig. 2.17) for the $^{70}(Ge)_{16}^{74}(Ge)_8$ "as-grown" superlattice as theoretically predicted [86]. We should underline that the excellent agreement between results of papers [87, 88].

In concluding this paragraph we should stressed that *isotopic superlattice* represents an excellent model system for the investigation of *confinement* of optical phonons. Both frequencies and relative intensities of the measured spectra are in

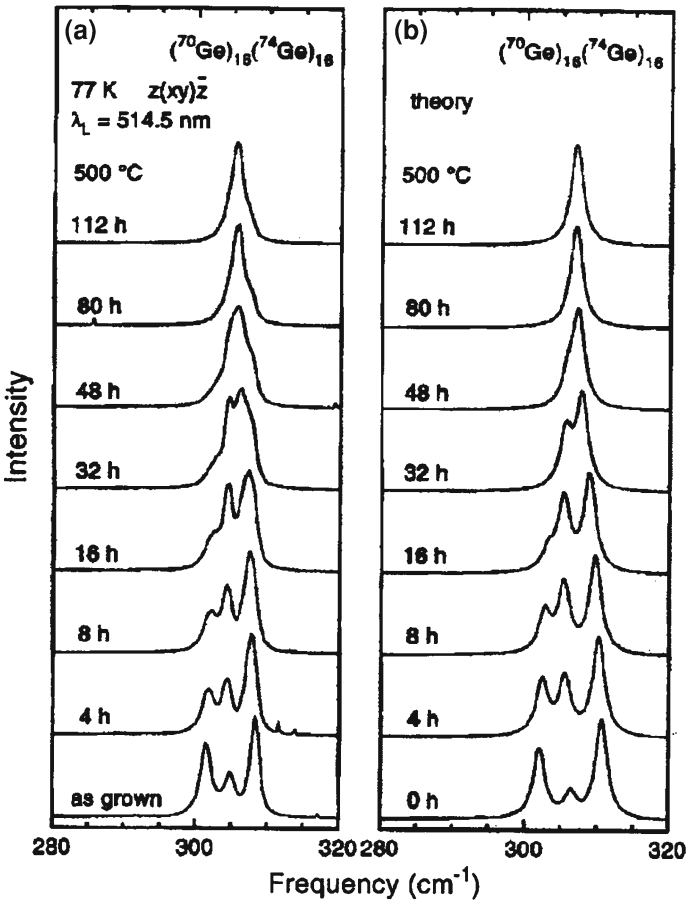

Fig. 2.17 **a** Experimental Raman spectra of a $(^{70}Ge)_{16}(^{74}Ge)_{16}$ superlattice for different annealing steps at 500°C. **b** Calculated Raman spectra for the same superlattice using the same parameters (after [88])

good agreement with calculations based on a planar *bond-charge model* and the bond-polarizability approach (for details see [93–95].

2.4 Excitons and Biexcitons in Quantum Dots

When a *semiconductor (insulator)* of *direct bandgap* E_g is shone with near-bandgap light, *electron-hole pairs* are created. If the electron and the hole were noninteracting only photon energies $\hbar\omega > E_g$ would be absorbed and E_g would be the absorption edge. The *Coulombic electron-hole interaction* greatly modifies this picture. The electron-hole attraction gives rise to bound states of the relative motion of the exciton.

The appearance of intense, narrow absorption lines below the fundamental absorption edge is the manifestation of these bound states.

In the case of confined systems for electrons and holes, such as *quantum wells (QWs), quantum wires (QWRs) and quantum dots (QDs)*, the *excitonic effects* are much more important than in *bulk solids*. In effect, as will be shown below, the binding energy of the electron- hole systems forming an excitons are much higher in quantum confined systems than in the case of solids, and, therefore, the excitonic transitions can be observed even at temperatures close to room temperature, as closed to the bulk case for which low temperatures are needed. This makes the role played by *excitons* in many optoelectronic devices of nanoscale very important.

It is perhaps easier to deal with a finite barrier *quantum dot* (QD) with spherical rather than cuboid symmetry. The approach is rather similar to that derived earlier for the circular *cross-section quantum wire* (QWr). Given the *spherical symmetry* of the potential, then the wave function would also be expected to have spherical symmetry, hence the Schrödinger equation for a constant *effective mass* could be written (see, e.g. [101, 103])

$$-\frac{\hbar^2}{2m^*}\left(\frac{\partial^2}{\partial x^2}+\frac{\partial^2}{\partial y^2}+\frac{\partial^2}{\partial z^2}\right)\Psi(r)+V(r)\Psi(r)=E_r\Psi(r), \tag{2.17}$$

where the index on E_r has been added just to indicate that this energy is associated with the *confinement* along the radius. In this case:

$$r=\sqrt{x^2+y^2+z^2}. \tag{2.18}$$

The transition can be made from Cartesian (x, y, z) to spherical polar coordinates, in effect just r, in the same way above. Using Eq. (93) of Ref. [102], each of the three *Cartesian axes* gives an equation of the following form:

$$\frac{\partial^2}{\partial x^2}\Psi(r)=\frac{1}{r}\frac{\partial}{\partial r}\Psi(r)-\frac{x^2}{r^3}\frac{\partial}{\partial r}\Psi(r)+\frac{x^2}{r^2}\frac{\partial^2}{\partial r^2}\Psi(r) \tag{2.19}$$

Therefore, the complete $\nabla^2\Psi(r)$ is given by:

$$\left(\frac{\partial^2}{\partial x^2}+\frac{\partial^2}{\partial y^2}+\frac{\partial^2}{\partial z^2}\right)\Psi(r) =\frac{3}{r}\frac{\partial}{\partial r}\Psi(r)-\frac{(x^2+y^2+z^2)}{r^3}\frac{\partial}{\partial r}\Psi(r)+\frac{(x^2+y^2+z^2)}{r^2}\frac{\partial^2}{\partial r^2}\Psi(r). \tag{2.20}$$

and

$$\left(\frac{\partial^2}{\partial x^2}+\frac{\partial^2}{\partial y^2}+\frac{\partial^2}{\partial z^2}\right)\Psi(r)=\frac{2}{r}\frac{\partial}{\partial r}\Psi(r)+\frac{\partial^2}{\partial r^2}\Psi(r). \tag{2.21}$$

Substituting into the Schrödinger equation then:

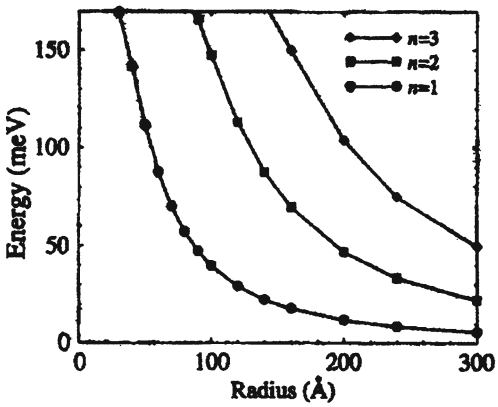

Fig. 2.18 The *confinement* energy in a *spherical* GaAs quantum dot surrounded by a $Ga_{0.8}Al_{0.2}As$ barrier (after [103])

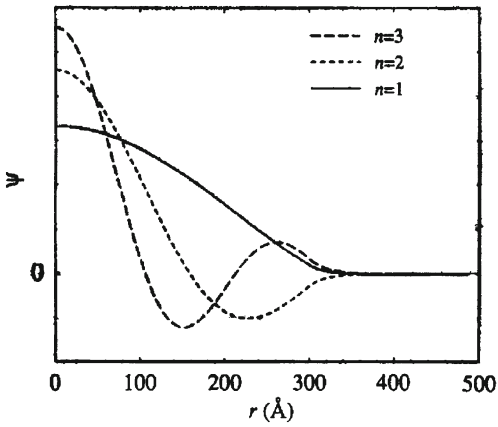

Fig. 2.19 The wave functions of the three lowest energy states in the 300 Å spherical quantum dot (after [103])

$$-\frac{\hbar^2}{2m^*}\left(\frac{2}{r}\frac{\partial}{\partial r}+\frac{\partial^2}{\partial r^2}\right)\Psi(r)+V(r)\Psi(r)=E_r\Psi(r). \tag{2.22}$$

Such spherical symmetric Schrödinger equations have been investigated before (see, e.g. [8–10]). The last equation, is numerically solved and Fig. 2.18 shows the results of calculations of the three lowest energy levels of a spherical GaAs QD surrounded by a finite barrier composed of $Ga_{0.8}Al_{0.2}As$, with a sharp boundary. In fact, the formalism above, as that of the *circular cross - section* QWr, is applicable for any radial potential profile V(r), e.g., it is also valid for diffused interfaces [103] Again, the behavior of the energies as a function of the spatial dimension, as shown in Fig. 2.18, is as expected in *confined* systems, namely the confinement energy decreases as the size of the system increases. Figure 2.19 displays the corresponding radial components of the wave functions. It can be seen that they all have a maximum at the centre of the potential and that as the principal quantum number n increases, then the number of nodes increases.

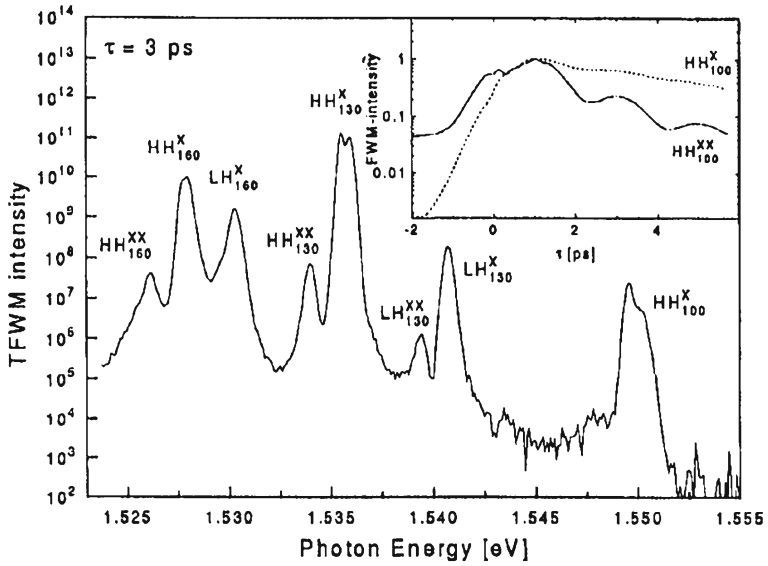

Fig. 2.20 Spectrally resolved four-wave mixing at $\tau = 3$ ps showing the heavy hole and light hole biexcitons. Insert shows the four-wave mixing intensity of the heavy hole exciton and biexciton as a function of delay (after [110])

In 1958, Moskalenko [104] and Lampert [105] suggested that in crystals besides excitons more complex electronic quasi particles might exist, made up of three or four carriers. The latter one, consisting of two electrons and two holes, is well known as *biexcitons* or *excitonic molecules* [106]. As the density of excitons is increased, biexcitons are formed by increasing the light intensity. Biexcitons can be generated either through ordinary excitation of the crystal or by two-photon absorption each photon having an energy

$$\mathrm{h}\nu = \mathrm{E}_x - \frac{\mathrm{E}_{B_{xx}}}{2}, \tag{2.23}$$

where $\mathrm{E}_{B_{xx}}$ is the *biexciton binding energy* and E_x is the *exciton energy*

$$\mathrm{E}_x = \mathrm{E}_\mathrm{g} - \mathrm{E}_{B_x} + \frac{\hbar^2 \mathrm{k}^2}{2\mathrm{m}_x}. \tag{2.24}$$

In the last relation E_g is the bandgap energy, E_{B_x} is the exciton binding energy and $\frac{\hbar^2 \mathrm{k}^2}{2\mathrm{m}_x}$ is the kinetic energy with which an exciton moves through the crystal (see, also [107]).

Compared to the bulk material, an increased stability of biexcitons due to the two-dimensional carrier confinement is observed for typical III–V structures such as GaAs/AlGaAs QWs [108–110] (see Fig. 2.20) or for wide bandgap II–VI materials such as CdZnSe/ZnSe [111]. As a consequence of the enhanced biexciton binding

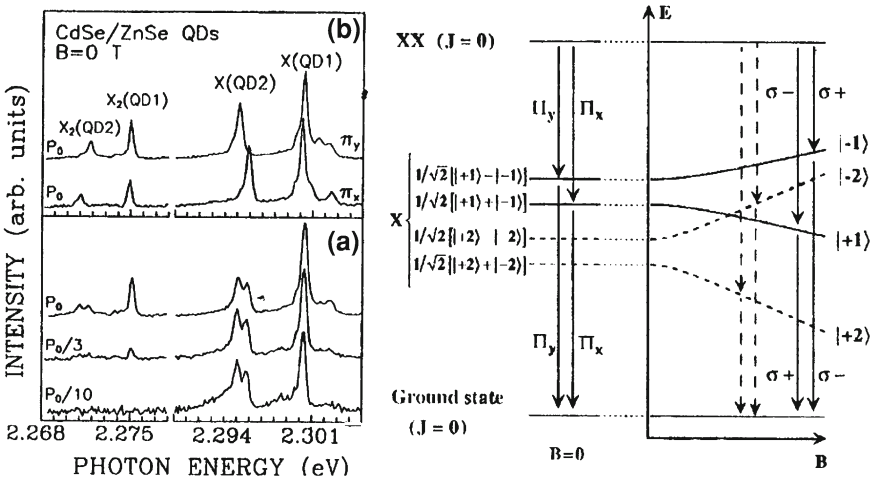

Fig. 2.21 *Left side Excitonic* (X) and *biexcitonic* (X_2) emission from two individual CdSe/ZnSe SQDs for different excitation powers. The PL spectra shown in the lower panel are unpolarized, the data presented in the upper panel represent linearly polarized PL spectra (π_x and π_y, respectively). *Right side* Energy level scheme for the biexciton–exciton cascade in a QD (after [111])

energy, a variety of optical properties, such as the photoluminescence(PL) spectrum, the optical gain or the four-wave mixing signal especially in wide bandgap II–VI QWs are strongly influenced by *biexcitons* (see [111] and references therein).

Below we briefly review some results obtained from *optical spectroscopy* on epitaxially grown single SQDs based on II–VI and II–N compounds. As was indicated above the biexciton (XX or X_2) is a four-particle state. In its lowest energy state configuration, two electrons and two holes with antiparallel spins occupy the first quantized state of the *conduction* and the *valence band* in the SQDs, respectively (see, e.g. [112]) We should add that the QDs in the material systems described here are quite small with diameters in the order of 10 nm and heights of a few nm. The biexciton state is therefore a singlet state with a total spin of $J = 0$. Thus, the exciton state X represents the final state for the biexciton recombination [113]. In II–VI semiconductors, as in III–V materials with a zincblende crystal lattice, *Coulomb interaction* leads to positive biexciton binding energies (see Eq. (2.24)), i.e., the energetic distance between XX (X_2) and X smaller than the energy difference between the first exciton state and the ground state. A typical optical fingeprint for the X_2 is therefore an additional PL line at the low energy side of the exciton *emission* X that exhibits a strong (quadratic) dependence on the excitation power [107]. This behavior is clearly visible in left panel of Fig. 2.21. At low excitation density, the PL spectrum of CdSe/ZnSe SQDs consists of emission peaks stemming from *exciton* recombination of two individual QDs. With rising excitation density additional lines emerge, red shifted by about 24 meV with respect to the excitonic emission X, and rapidly increasing in intensity, which can be attributed to biexciton emission X_2. The biexciton binding energy is obviously much larger than in III. As-based QDs

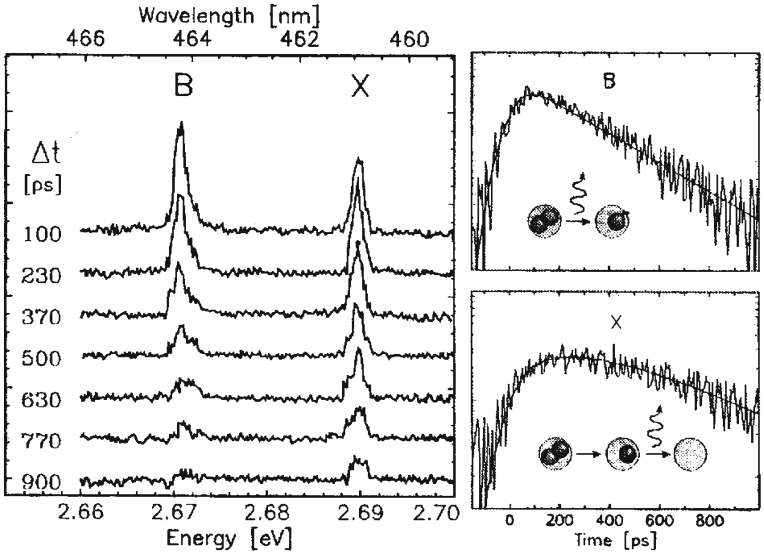

Fig. 2.22 *Left panel* Transient PL spectra from a single CdSe/ZnSe QD showing the single exciton X and the *biexciton* transition (here denoted by B = X_2). *Right panel* Decay curves for the exciton and the biexciton PL signal (for details see text) (after [111])

where a typical values of a few meV (∼2 meV [110]) have been determined (see, also [108, 109, 114]). When having a closer look on the PL spectra presented in Fig. 2.21, some more information can be extracted. One should have in mind that in QDs, the light hole level is shifted to higher energies due to strain and *confinement* and thus, excitons are formed between electrons and heavy holes. The ground state of a heavy hole exciton in a SQD is a spin quadruplet, which can be by the z-component (= component, according [111] in growth direction) of the total exciton spin J_z. If the z-component of the electron spin, $s_z = \pm$ 1/2, and the z-component of the total angular momentum of the heavy hole $j_z = \pm$ 3/2 are antiparallel, in such case, we get $J_z = s_z + j_z = \pm 2$ (the *dark exciton states* [113]).

In II–VI QDs the energy difference Δ_0 between *bright and dark exciton states* that is given by the isotropic electron-hole interaction energy, amounts to about 1 meV and more which is nearly an order of magnitude larger than in InAs/GaAs QDs [101]. As can be seen in Fig. 2.21, the exciton fine structure is reflected both in the exciton and in the biexciton recombination: SQD1 does not show a significant splitting of the exciton PL signal, while SQD2 exhibits a doublet with an energy separation of almost 1 meV indicating a reduced QD symmetry. Exactly the same behavior is observed in the corresponding biexciton lines. Moreover, the high energy component of the X emission in SQD2 (π_x polarized) corresponds to the low energy component of the X_2 emission and vice versa, in agreement with energy level scheme (see Fig. 2.20). All these effects are easily accessible in wide bandgap II–VI QDs because the characteristic energy splitting are significantly enhanced with respect to

III-As semiconductor QDs. We may expect more significant value of the exchange splitting for exciton and biexciton states in QD of *isotope-mixed crystals* (see, also [60, 93–95]). Thanks to the large biexciton binding energy, II–VI QDs were the first, where the biexciton–exciton cascade could be traced directly in the time domain on SQD level [115]. Figure 2.22 depicts transient PL spectra (left) of both *emission* lines and the time-dependent intensity of the exciton and the biexciton signal (right panel). The biexciton emission shows a monoexponential decay with a time constant of 310 ps. The exciton reveals a more complex behavior: the onset of the exciton line ids delayed, resulting in "plateau-like" characteristics of the exciton decay curve. The excitation density according authors of this experiment was set to a value where an average number of two electron-hole pairs per excitation pulse in the SQD was generated. Model calculations taking into account the biexciton state, the *bright*, and the *dark exciton states* and the "empty" QD (corresponding to a QD population with 2, 1 and 0 excitons, respectively) confirm that the exciton state is feeded by the biexciton recombination causing the delayed onset and the "plateau-like" characteristics of the *exciton emission dynamics* (for details see [101] and references therein).

References

1. F. Soddy, Intra-atomic charge. Nature (London) **92**, 399–400 (1913)
2. F. Soddy, The structure of the atom. Nature (London) **92**, 452–452 (1913)
3. H. Frauenfelder, E.M. Henley, *Subatomic Physics* (Prentice Hall, New York, 1991)
4. J.J. Kelly, Nucleon charge and magnerization densities from Sachs form factors. Phys. Rev. **C66**, 065203–065206 (2002)
5. G.A. Miller, A.K. Opper, E.J. Stephenson, Charge symmetry breaking and QCD, ArXiv: nucl-ex/0602021
6. G.A. Miller, Charge densities of the neutron and proton. Phys. Rev. Lett. **99**, 112001–112004 (2007)
7. G.A. Miller, J. Arringfton, The neutron negative central charge density: an inclusive–exclusive connection, ArXiv: nucl-th/0903.1617
8. P.A.M. Dirac, *The Principles of Quantum Mechanivs* (Oxford University Press, UK, 1958)
9. R.P. Feyman, R.P. Leighton, M. Sands, *The Feyman Lecture in Physics*, vol. 3 (Addison Wesley, Reading, MA, 1965)
10. L.D. Landau, E.M. Lifshitz, *Quantum Mechanics (Nonrelativistic Theory)* (Pergamon, New York, 1977)
11. V.G. Plekhanov, Manifestation and origin of the isotope effect, ArXive: gen. phys/0907.2024 (2009) pp. 1–192
12. F.W. Aston, *Mass-Spectra and Isotopes* (Science, Moscow, 1948). (in Russian)
13. K. Blaum, High accuracy mass spectrometry with stored ions. Phys. Reports **425**, 1–783 (2006)
14. K. Blaum, W. Geithnar, J. Lassen, Nuclear moments and charge radii of argon isotopes between the neutron-shell closures N = 20 and N = 28, Nucl. Phys. **799**, 30–45 (2008)
15. M. Glaser, M. Borys, Precision mass measurements. Rep. Prog. Phys. **72**, 126101–126131 (2009)
16. S.M. Wong, *Introductory Nuclear Physics* (Wiley, New York, 1998)
17. Ju.M. Schirokov, N.P. Judin, *Nuclear Physics* (Science, Moscow, 1980). (in Russian)
18. W.F. Hornyack, *Nuclear Structurs* (Academic Press, New York, 1975)
19. B.M. Brink, *Nuclear Forces* (Pergamon, New York, 1965)

20. J. Carlson, R. Schiavilla, Structure and dynamics of few—nucleon systems. Rev. Mod. Phys. **70**, 743–841 (1998)
21. C. Davies, S. Collins, Physics, (World, August, 2000), pp. 35–40
22. V.G. Plekhanov, Isotope effect on the lattice dynamics in crystals. Mater. Sci. Eng. **R35**, 139–237 (2001)
23. I.M. Lifshitz, *Selected Papers Physics of Real Crystals and Disordered Systems* (Science, Moscow, 1987). (in Russian)
24. A.A. Maradudin, E.W. Montroll, G.H. Weiss, I.P. Iopatova, *Theory of Lattice Dynamics in the Harmonic Approximation* (Academic Press, New York, 1971)
25. M. Born, K. Huang, *Dynamical Theory of Crystal Lattice* (Oxford University Press, London, 1968)
26. V.G. Plekhanov, Lattice-dynamics of isotope-mixed crystals, ArXiv: cond-mat/1007.5125 (2010)
27. G. Dolling, in *Neutron Spectroscopy and Lattice Dynamics*, ed. by G.K. Horton, A.A. Maradudin, Dynamical Properties of Solids, vol 1, (North-Holland, Amsterdam, 1974) Chap. 10, pp. 543–629
28. G. Dolling, A.D.B. Woods, *Thermal Vibrations Crystal Lattice*, in ed. by P.A. Egelstaff, Thermal Neutron Scattering, (Academic Press, New York, 1965), pp. 178–262
29. A.S. Barker Jr, A.J. Sievers, Optical studies of the vibrational properties of disordered solids. Rev. Mod. Phys. **47**(Suppl. 2), S1–S179 (1975)
30. R.J. Elliott, J.A. Krumhansl, P.L. Leath, The theory and properties of randomly disordered crystals and physical systems. Rev. Mod. Phys. **46**, 465–542 (1974)
31. R.J. Elliott, I.P. Ipatova (eds.), *Optical Properties of Mixed Crystals* (North-Holland, Amsterdam, 1988)
32. I.P. Ipatova, Universal parametrs in mixed crystals in [30] Chap. 1, pp. 1–34
33. D.W. Taylor, Phonon response theory and the infrared and Raman experiments in [30] Chap. 2, pp. 35–132
34. M. Lax, E. Burstein, Infrared lattice absorption in ionic and homopolar crystals. Phys. Rev. **97**, 39–52 (1955)
35. V.F. Agekyan, A.M. Asnin, V.M. Kryukov et al., Isotope effect in germanium, Fiz. Tverd. tela (St. Petersburg) **31**, 101–104, (1989). (in Russian)
36. H.D. Fuchs, G.H. Grein, C. Thomsen et al., Comparison of the phonon spectra of ^{70}Ge and ^{nat}Ge crystals: effects of isotopic disorder. Phys. Rev. **B43**, 483–491 (1991)
37. H.D. Fuchs, S.H.Grein, R.I. Devlen, et al., Anharmonic decay time, isotopic scattering time, and inhomogeneous line broadening optical phonons in ^{70}Ge, ^{76}Ge and natural Ge crystals ibid **B44**, 8633–8642, (1991)
38. P.W. Andersen, Absence of diffusion in certain random lattice. Phys. Rev. **109**, 1492–1505 (1955)
39. P.W. Andersen, Solid state physics **2**, 193–243, 1970
40. P. Etchegoin, H.D. Fuchs, J. Weber et al., Phonons in isotopically disordered Ge. Phys. Rev. **B48**, 12661–12671 (1993)
41. J.M. Zhang, M. Giehler, A. Gobel et al., Optical phonons in isotopic Ge studied by Raman scattering. Phys. Rev. **B57**, 1348–1351 (1998)
42. J.M. Zhang, T. Ruf, R. Lauck et al., Raman spectra of isotopic GaN. Phys. Rev. **B56**, 14399–14404 (1997)
43. H. Hanzawa, N. Umemura, Y. Nisida, H. Kanda, Disorder effect of nitrogen impurities, irradiation-induced defects and ^{13}C isotope composition on the Raman spectrum in synthetic I^b diamond, Phys. Rev. **B54**, 3793–3799 (1996)
44. F. Widulle, T. Ruf, M. Konuma et al., Isotope effects in elemental semiconductors: a Raman study of silico. Solid State Commun. **118**, 1–22 (2001)
45. D.T. Wang, A. Gobel, J. Zepenhagen, et al., Raman scattering on α-Sn: dependence on isotopic composition, Phys. Rev. **B56**, 13167–13 171, (1997)
46. F. Widulle, *Raman spectroscopy of semiconductors with controlled isotopic composition* (Ph. D, Stuttgart, Germany, 2002)

47. V.G. Plekhanov, Isotope effects in lattice dynamics. Physics-Uspekhi **46**, 689–715 (2003)
48. K.C. Hass, M.A. Tamor, T.R. Anthony, W.F. Banholzer, Lattice dynamics and Raman spectra of isotopically mixed diamond. Phys. Rev. **B45**, 7171–7182 (1992)
49. J. Spitzer, P. Etchegoin, T.R. Anthony et al., Isotopic—disorder induced Raman scattering in diamond. Solid State Commun. **88**, 509–513 (1983)
50. R.M. Chrenko, ^{13}C-doped diamond: Raman spectra. Appl. Phys. **63**, 5873–5875 (1988)
51. V.G. Plekhanov, *Giant Isotope Effect in Solids* (Stefan University Press, La Jolla, 2004)
52. M. Schwoerer-Bohning, D.A. Arms, A.T. Macrander, Phonon dispersion of diamond measured by inelastic X-ray scattering. Phys. Rev. Lett. **80**, 5572–5575 (1998)
53. S.A. Solin, A.K. Ramdas, Raman spectrum of diamond. Phys. Rev. **B1**, 1687–1699 (1970)
54. V.G. Plekhanov, Experimental evidence of strong scattering in isotopical disordered systems: the case LiH_xD_{1-x}. Phys. Rev. **B51**, 8874–8878 (1995)
55. V.G. Plekhanov, Experimental evidence of strong scattering in isotopical disordered systems, ArXiv: cond-mat/0907.3817
56. V.G. Plekhanov, Lattice dynamics of isotopically mixed systems, Opt. Spectr. (St. Petersburg) **82**, 95–124, 69 (1997)
57. V.G. Plekhanov, Isotopic and disorder effects in large exciton spectroscopy, Uspekhi-Phys. (Moscow) **167**, 577–604, (1997). (in Russian)
58. A.F. Kapustinsky, L.M. Shamovsky, K.S. Bayushkina, Thermochemistry of isotopes. Acta physicochem (USSR) **7**, 799–810 (1937)
59. A.A. Klochikhin, Renormalization of Wannier–Mott exciton spectrum by Fr chlich interaction. Sov. Phys. Solid State **22**, 986–992 (1980)
60. V.G. Plekhanov, Elementary excitations in isotope-mixed crystals. Phys. Reports **410**, 1–235 (2005)
61. Y. Onodera, Y. Toyozawa, Persistence and amalgamation types in the electronic structure of mixed crystals. J. Phys. Soc. Japan **24**, 341–355 (1968)
62. Y. Toyozawa, *Optical Processes in Solids* (Cambridge University Press, Cambridge, 2003)
63. F.I. Kreingol'd, K.F. Lider, K.I. Solov'ev, Isotope shift of exciton line in absorption spectrum Cu_2O, JETP Letters (Moscow) **23**, 679–681, (1976). (in Russian)
64. F.I. Kreingol'd, K.F. Lider, V.F. Sapega, Influence of isotope substitution on the exciton spectrum in Cu_2O crystal, Fiz. Tverd. Tela **19**, 3158–3160, (1977). (in Russian)
65. F.I. Kreingol'd, B.S. Kulinkin, Influence of isotope substitution on the forbidden gap of ZnO crystals, ibid **28**, 3164–3166, (1986). (in Russian)
66. F.I. Kreingol'd, Dependence of band gap ZnO on zero-point energy, ibid **20**, 3138–3140, (1978). (in Russian)
67. F.I. Kreingol'd, K.F. Lider, M.B. Shabaeva, Influence of isotope substitution sulfur on the exciton spectrum in CdS crystal, ibid, **26**, 3940–3941, (1984). (in Russian)
68. J.M. Zhang, T. Ruf, R. Lauck et al., Sulfur isotope effect on the excitonic spectra of CdS. Phys. Rev. **B57**, 9716–9722 (1998)
69. T.A. Meyer, M.L.W. Thewalt, R. Lauck et al., Sulfur isotope effect on the excitonic spectra of CdS. Phys. Rev. **B69**, 115214–5 (2004)
70. D. Karaskaja, M.L.W. Thewalt, T. Ruf, Photoluminescence studies of isotopically-enriched silicon: Isotopic effects on indirect electronic band gap and phonon energies. Solid State Commun. **123**, 87–92 (2003)
71. D. Karaskaja, M.L.W. Thewalt, T. Ruf, Phys. Stat. Sol. (b) **235**, 64–69 (2003)
72. S. Tsoi, H. Alawadhi, X. Lu et al., Electron–phonon renormalization of electronic bandgaps of semiconductors: Isotopically enriched silicon. Phys. Rev. **B70**, 193201–193204 (2004)
73. A.K. Ramdas, S. Rodriguez, S. Tsoi et al., Electronic band gaps of semiconductors as influenced by their isotopic composition. Solid State Commun. **133**, 709–714 (2005)
74. S. Tsoi, S. Rodriguez, A.K. Ramdas et al., Isotopic dependence of the E_0 and E_1 direct gaps in the electronic band structure of Si. Phys. Rev. **B72**, 153203–4 (2005)
75. H. Kim, S. Rodriguez, T.R. Anthony, Electronic transitions of holes bound to boron acceptors in isotopically controlled diamond. Solid State Commun. **102**, 861–865 (1997)

76. A.A. Klochikhin, V.G. Plekhanov, Isotope effect on the Wannier–Mott exciton levels. Sov. Phys. Solid State **22**, 342–344 (1980)
77. V.G. Plekhanov, Direct observation of the effect of isotope-induced-disorder on the exciton binding energy in LiH_xD_{1-x} mixed crystals. J. Phys. Condens. Matter **19**, 086221–9 (2007)
78. V.G. Plekhanov, Isotopetronics-new direction of nanoscience, ArXiv: gen. phys/1007.5386
79. A. Cho (ed.), *Molecular Beam Epitaxy* (Springer, Berlin, 1997)
80. G.B. Stringfellow, *Organometallic Vapor—Phase Epitaxy: Theory and Practice*, 2nd edn. (Academic Press, London, 1999)
81. M.J. Kelly, *Low-Dimensional Semiconductors* (Clarendon Press, Oxford, 1995)
82. J.H. Davis, *The Physics of Low-Dimensional Semiconductors* (Cambridge University Press, Cambridge, 1998)
83. K. Goser, P. Glsektter, J. Dienstuhl, *Nanoelectronics and Nanosystems* (Springer, Berlin, 2004)
84. A.A. Berezin, Isotope superlattices and isotopically ordered structures. Solid State Commun. **65**, 819–821 (1988)
85. E.E. Haller, Isotope heterostructures selectively doped by neutron transmutation. Semicond. Sci. & technol. **5**, 319–321 (1990)
86. M. Cardona, P. Etchegoin, H.D. Fuchs et al., Effect of isotopic disorder and mass on the electronic and vibronic properties of three-, two- and one- dimensional solids. J. Phys. Condens Matter **5**, A61–A72 (1993)
87. J. Spitzer, T. Ruf, W. Dondl et al., Raman scattering by optical phonons in isotopic $^{70}(Ge)_n^{74}(Ge)_n$ superlattices. Phys. Rev. Lett. **72**, 1565–1568 (1994)
88. E. Silveira, W. Dondl, G. Abstreiter et al., Ge self - diffusion in isotopic $^{70}(Ge)_n^{74}(Ge)_m$ superlattices: A Raman study. Phys. Rev. **B56**, 2062–2069 (1997)
89. M. Nakajima, H. Harima, K. Morita, et al., Coherent confined LO phonons in $^{70}Ge/^{74}Ge$ isotope superlattices generated by ultrafast laser pulses, Phys. Rev. **B63**, 161304(R)(1–4) (2001)
90. V.G. Plekhanov, Applications of isotope effects in solids. J. Mater. Science **38**, 3341–3429 (2003)
91. A.V. Kolobov, K. Morita, K.M. Itoh et al., A Raman scattering study of self-assembled pure isotope Ge/Si (100) quantum dots. Appl. Phys. Lett. **81**, 3855–3857 (2002)
92. T. Kojima, R. Nebashi, Y. Shiraki et al., Growth and characterization of $^{28}Si/^{30}Si$ isotope superlattices. Appl. Phys. Lett. **83**, 2318–2320 (2003)
93. L.M. Zhuravleva, V.G. Plekhanov, Nuclear technology in creation of low-dimensional isotope-mixed structures. Nanoind. **4**, 28–30, (2009). (in Russian)
94. http://www.nanoindustry.su
95. L.M. Zhuravleva, V.G. Plekhanov, Isotopetronics and quantum information, Nano microsyst. **N3**, 46–54, (2011). (in Russian)
96. M. Cardona, M.L.W. Thewalt, Isotope effect on the optical spectra of semiconductors. Rev. Mod. Phys. **77**, 1173–1224 (2005)
97. M.A. Herman, W. Richter, H.Sitter, *Epitaxy, Physical Principles and Technical Implementation*, in Springer Series in Materials Science, vol. 62 (Springer, Heidelberg, 2004)
98. V.G.Plekhanov, *Isotope-Mixed Crystals: Fundamentals and Applications* (2011, in press)
99. G. Fasol, M. Tanaka, H. Sakaki et al., Interface roughness and dispersion of confined LO phonons in GaAs/AlAs quantum wells. Phys. Rev. **B38**, 6056–6065 (1988)
100. H. Bilz, W. Kress, *Phonon Dispersion Relations in Insulators* (Springer, Berlin, 1979)
101. P. Michler (ed.), *Single Semiconductor Quantum Dots* (Springer, Berlin, 2009)
102. K. Barnham, D. Vvedensky, *Low-Dimensional Semiconductor Structures* (Cambridge University Press, Cambridge, 2009)
103. P. Harrison, *Quantum Wells, Wires, and Dots* (Wiley, New York, 2001)
104. S.A. Moskalenko, Towards to theory of Mott excitons in alkali halides crystals, Opt. Spectr. **5**, 147–155, (1958) (in Russian)
105. M.A. Lampert, Mobile and immobile effective-mass-particle complexes in nonmetallic solids. Phys. Rev. Lett. **1**, 450–453 (1958)

106. V.G. Plekhanov, Fundamentals and applications of isotope effect in solids. Progr. Mat. Science **51**, 287–426 (2006)
107. B. Hnerlage, R. Levy, J.B. Grun et al., The dispersion of excitons, polaritons and biexcitons in direct-gap semiconductors. Phys. Reports **124**, 163–253 (1985)
108. R.C. Miller, D.A. Kleinman, W.T. Tsang, Observation of the excited level of excitons in GaAs quantum wells. Phys. Rev. **B24**, 1134–1136 (1981)
109. R.C. Miller, D.A. Kleinman, W.T. Tsang, Observation of the excited level of excitons in GaAs quantum wells, ibid **B25**, 6545–6549, (1982)
110. D. Birkedal, J. Singh, V.G. Lyssenko et al., Binding of quasi two-dimensional biexcitons. Phys. Rev. Lett. **76**, 672–675 (1996)
111. G. Bacher, T. Kmmel, Optical properties of epitaxially grown wide bandgap single quantum dots, in [101] pp. 71–121
112. V.G. Plekhanov, Isotope—based quantum information, ArXiv:quant-ph/0909.0820 (2009)
113. G. Chen, T.H. Stievater, E.T. Batteh et al., Biexciton quantum coherence in a single quantum dot. Phys. Rev. Lett. **88**, 117901–117904 (2002)
114. Special issue on high excitation and short pulse phenomena, J. Luminesc. **30**, N1–4 (1985)
115. K. Herz, T. Kmmel, G. Bacher et al., Biexcitons in low-dimensional CdZnSe/ZnSe structures. Phys. Stat. Solidi (a) **164**, 205–208 (1997)

http://www.springer.com/978-3-642-28749-7

Isotope-Based Quantum Information
G. Plekhanov, V.
2012, X, 129 p. 62 illus., Softcover
ISBN: 978-3-642-28749-7